Monthly Notices
of the
ROYAL ASTRONOMICAL SOCIETY

MNRAS **463,** 3365–3380 (2016)
Advance Access publication 2016 September 5

doi:10.1093/mnras/stw2217

RoboPol: the optical polarization of gamma-ray-loud and gamma-ray-quiet blazars

E. Angelakis,[1★] T. Hovatta,[2,3] D. Blinov,[4,5,6] V. Pavlidou,[4,6] S. Kiehlmann,[2,3] I. Myserlis,[1] M. Böttcher,[7] P. Mao,[8] G. V. Panopoulou,[4,6] I. Liodakis,[4,6] O. G. King,[9] M. Baloković,[9] A. Kus,[10] N. Kylafis,[4,6] A. Mahabal,[9] A. Marecki,[10] E. Paleologou,[4,6] I. Papadakis,[4,6] I. Papamastorakis,[4,6] E. Pazderski,[11] T. J. Pearson,[9] S. Prabhudesai,[11] A. N. Ramaprakash,[11] A. C. S. Readhead,[9] P. Reig,[4,6] K. Tassis,[4,6] M. Urry[8] and J. A. Zensus[1]

[1]*Max-Planck-Institut für Radioastronomie, Auf dem Hügel 69, D-53121 Bonn, Germany*
[2]*Aalto University, Metsähovi Radio Observatory, Metsähovintie 114, FI-02540 Kylmälä, Finland*
[3]*Department of Radio Science and Engineering, Aalto University, PO Box 13000, FI-00076 Aalto, Finland*
[4]*Department of Physics and Institute of Theoretical and Computational Physics, University of Crete, 71003 Heraklion, Greece*
[5]*Astronomical Institute, St. Petersburg State University, Universitetsky pr. 28, Petrodvoretz, 198504 St. Petersburg, Russia*
[6]*Foundation for Research and Technology – Hellas, IESL, 7110 Heraklion, Greece*
[7]*North-West University, Potchefstroom Campus, Private Bag X6001, Potchefstroom 2520, South Africa*
[8]*Yale Center for Astronomy & Astrophysics, Physics Department, New Haven, CT 06520, USA*
[9]*Cahill Center for Astronomy and Astrophysics, California Institute of Technology, 1200 E California Blvd, MC 249-17, Pasadena, CA 91125, USA*
[10]*Toruń Centre for Astronomy, Faculty of Physics, Astronomy and Informatics, Nicolaus Copernicus University, Grudziadzka 5, PL-87-100 Toruń, Poland*
[11]*Inter-University Centre for Astronomy and Astrophysics, Post Bag 4, Ganeshkhind, Pune 411 007, India*

Accepted 2016 September 1. Received 2016 September 1; in original form 2016 April 27

ABSTRACT

We present average *R*-band optopolarimetric data, as well as variability parameters, from the first and second RoboPol observing season. We investigate whether gamma-ray-loud and gamma-ray-quiet blazars exhibit systematic differences in their optical polarization properties. We find that gamma-ray-loud blazars have a systematically higher polarization fraction (0.092) than gamma-ray-quiet blazars (0.031), with the hypothesis of the two samples being drawn from the same distribution of polarization fractions being rejected at the 3σ level. We have not found any evidence that this discrepancy is related to differences in the redshift distribution, rest-frame *R*-band luminosity density, or the source classification. The median polarization fraction versus synchrotron-peak-frequency plot shows an envelope implying that high-synchrotron-peaked sources have a smaller range of median polarization fractions concentrated around lower values. Our gamma-ray-quiet sources show similar median polarization fractions although they are all low-synchrotron-peaked. We also find that the randomness of the polarization angle depends on the synchrotron peak frequency. For high-synchrotron-peaked sources, it tends to concentrate around preferred directions while for low-synchrotron-peaked sources, it is more variable and less likely to have a preferred direction. We propose a scenario which mediates efficient particle acceleration in shocks and increases the helical *B*-field component immediately downstream of the shock.

Key words: polarization – galaxies: active – galaxies: jets – galaxies: nuclei.

1 INTRODUCTION

Active galactic nuclei (AGNs) are the small fraction of galaxies (∼7 per cent; Roy 1995) that appear to have nuclear emission exceeding or comparable to the total stellar output. Of all members of the AGN class, 'blazars' are both the most variable sources and the sources that are most common in the gamma-ray sky (Nolan et al. 2012; Acero et al. 2015). With defining characteristic the close alignment of their confined plasma flow to our line of sight and the often relativistic speeds involved (Blandford & Königl 1979), their jet dominates the emission, generally outshining the host galaxy.

★ E-mail: eangelakis@mpifr.de

Blazars emit radiation throughout the electromagnetic spectrum – through synchrotron at lower frequencies, and through inverse Compton, and possibly hadronic processes, at high frequencies. Owing to its synchrotron character, the blazar jet emission at energies around and below optical frequencies is expected to be polarized. The polarization levels depend mostly on the degree of uniformity of the magnetic field at the emission element (Pacholczyk 1970). The mere detection of some degree of polarization already implies some degree of uniformity in the magnetic field (e.g. Sazonov 1972) and provides a handle for understanding its topology and strength at the source rest frame, assuming that the polarized radiation transmission can be modelled accurately.

In blazars, both the linear polarization degree and angle can show variations over a range of time-scales and magnitudes (Strittmatter et al. 1972; Yuan et al. 1998; Uemura et al. 2010). The polarization angle often goes through phases of monotonic transition ('rotations') between two limiting values (Kikuchi et al. 1988). The detection of such events that specifically appeared to be associated with episodic activity at high energies (Marscher et al. 2008, 2010; Abdo et al. 2010; Aleksić et al. 2014) prompted the use of rotations as a tool to probe the inner regions of AGN jets and gave rise to a series of different scenarios about the physical processes that may be causing them.

In order to pursue a systematic investigation of optical polarization properties and the polarization plane rotations of blazars, we initiated the RoboPol high-cadence polarization monitoring programme (King et al. 2014; Pavlidou et al. 2014). The aim of the programme is to study an unbiased subset of a photon-flux-limited sample of gamma-ray-loud (GL) AGNs, as well as smaller 'control' sample of gamma-ray-quiet (GQ) blazars. The main scientific questions that the programme was designed to address are as follows.

(i) Do temporal coincidences between activity at high energies and polarization rotations indeed imply a physical connection between the events?
(ii) What is the temporal polarimetric behaviour of blazars?
(iii) Do the optical polarization properties of GL and GQ blazars differ in a systematic fashion? And are the optical polarization and gamma-ray emission independent, or driven by the same process and hence causally connected?

First results on the first two questions have been presented in Blinov et al. (2015, 2016a). In this paper, we focus on the third question: the optopolarimetric differences between GL and GQ blazars. On the basis of the exploratory observations conducted during and shortly after the instrument commissioning (2013 May–July; Pavlidou et al. 2014, hereafter Survey Paper), we found a significant difference (3σ level) in the values of the polarization fraction between GL and GQ sources as measured in a single-epoch survey. The current paper uses data from the first two RoboPol observing seasons to verify whether there is indeed a divergence between the two samples and investigate what may be causing it.

The paper is organized as follows: Section 2 briefly discusses the blazar samples and observations used in this work. The higher level data products that we use are presented in Section 3 along with the maximum-likelihood methods used in the estimation of intrinsic mean values. In Section 4, we present a number of studies aiming at investigating the possible dependence of the polarization on other source properties. In the same section, we test for consistency of polarimetric properties between GL and GQ sources. Finally, in Section 5 we summarize and discuss our findings within the framework of a shock-in-jet model.

2 SOURCE SAMPLE AND OBSERVATIONS

The details of the source sample selection are discussed in the Survey Paper as well as in Blinov et al. (2015). The GL sample that was monitored during the first two seasons ('main' GL sample, 62 sources) is a subset of a photon-flux-limited sample of blazars (557 GL sources) from the *Fermi*-LAT Second Source Catalog (2FGL; Nolan et al. 2012), to which we applied an *R*-band flux cut as well as bias-free cuts related to visibility from Skinakas and field quality such as proximity of other field sources.

Richards et al. (2011) have shown that GQ sources have lower radio modulation indices. Therefore, we select the GQ sample ('main' GQ sample, 15+2 sources) from the source sample of the 15 GHz Owens Valley Radio Observatory (OVRO) blazar monitoring programme (Richards et al. 2011) based on radio variability properties and absence from the 2FGL. The selected sources have 15 GHz flux density above 60 mJy and a modulation index higher than 0.02. Additionally, the same *R*-band flux, visibility, and field-quality cuts have been applied to the GQ sample as to the GL sample. Two of the original GQ sources (cf. Survey Paper) – RBPLJ1624+5652 and RBPLJ1638+5720 – appear in the *Fermi*-LAT 4-year Point Source Catalog (3FGL; Acero et al. 2015). These sources have been replaced by two new control sources.

In Table 1, we list the GL and GQ sources observed at least once during the first two seasons. In each of the following studies, we include any source from that list that satisfies all the requirements relevant to that study, independently of whether it was monitored or not. The requirements relevant to each study are stated in the corresponding section.

The data sets presented here have been acquired during the first two RoboPol monitoring seasons, which followed a brief commissioning phase (2013 May–July; King et al. 2014; Survey Paper). The first season lasted from 2013 May 26 until 2013 November 27 with 67 per cent of the observing time usable; the second season lasted from 2014 April 11 till 2014 November 19 with about 60 per cent of the nights usable. Data-taking during each season is discussed in Blinov et al. (2015, 2016a), respectively, while our data processing and reduction pipeline is presented in detail in King et al. (2014). The pipeline output includes fractional Stokes parameters q ($q = Q/I$) and u ($u = U/I$) and their uncertainties, from which the linear polarization fraction p and the electric vector position angle (EVPA) χ for each source are calculated, with their uncertainties derived from error propagation (see equations 5 and 6 in King et al. 2014).

The median uncertainties of q and u from all measurements in our data set that passed the quality criteria are both around 0.007 while that of the polarization angle χ is $4\overset{\circ}{.}7$. The median uncertainty in photometry based, for example, on PTF (Ofek et al. 2012) standard stars, is around 0.02 mag. A measure of the instrumental polarization is given by table 1 in King et al. (2014), where it is shown that the mean absolute difference between RoboPol-measured and catalogued degree of polarization for polarized standard stars is about $(3 \pm 5) \times 10^{-2}$ in terms of polarization fraction p. Finally, the instrumental rotation is $2\overset{\circ}{.}31 \pm 0\overset{\circ}{.}34$.

After the pipeline operation and before any useful data product is processed, each measurement is subjected to post-reduction quality checks, which include the following.

(i) Goodness of the astrometry, by comparing the expected source position to that recovered from the reversal of the '1-to-4' mapping of the source. The tolerance is 9 arcsec.
(ii) Field 'crowdedness', which affects the reliability of the aperture photometry.

Table 1. Summary of the GL and GQ sources that were observed at least once during the first two RoboPol seasons. For each study we present here, we use the subset of the table that satisfies the relevant requirements. Columns (1) and (7) the RoboPol ID; (2) and (8) source survey name; (3) and (9) mark whether the source is in the TeV RoboPol or the F-GAMMA programme; (4) and (10) the 2FGL classification; (5) and (11) source redshift; (6) and (12) number of measurements.

ID (RBPL...)	Survey ID	Other[a]	Class[b]	z	N	ID (RBPL...)	Survey ID	Other[a]	Class[b]	z	N
	Monitored GC sources										
J0045+2127	GB6J0045+2127		bzb	...	23	J2340+8015	TXS2331+073		bzq	0.401	13
J0114+1325	GB6J0114+1325		bzb	2.025	20	J2334+0736	BZB	J2340+8015	bzb	0.274	18
J0136+4751	OC457	F2	bzq	0.859	24						
J0211+1051	BZBJ0211+1051		bzb	0.2	25		*Not monitored GL sources*				
J0217+0837	ZS0214+083		bzb	0.085	24	J0136+3905	B30133+388	TeV	bzb	...	4
J0259+0747	PKS0256+075		bzq	0.893	15	J0221+3556	S40218+35	F2	bzq	0.9440	1
J0303-2407	PKS0301-243		bzb	0.26	6	J0222+4302	3C66A		bzb	0.4440	24
J0405-1308	PKS0403-13		bzq	0.571	5	J0238+1636	AO0235+164	F12	bzb	0.9400	19
J0423-0120	PKS0420-01	F12	bzq	0.915	6	J0340-2119	PKS0338-214		bzb	0.2230	1
J0841+7053	4C71.07	F12	bzq	2.218	13	J0336+3218	NRAO140	F1	bzq	1.2630	6
J0848+6606	GB6J0848+6605		bzb	...	14	J0339-0146	PKS0336-01	F1	bzq	0.8520	4
J0957+5522	4C55.17		bzq	0.899	4	J0407+0742	TXS0404+075		bzq	1.1330	1
J0958+6533	S40954+65	F12	bzb	0.367	9	J0442-0017	PKS0440-00		bzq	0.8450	12
J1037+5711	GB6J1037+5711		bzb	0.8304	16	J0510+1800	PKS0507+17		bzq	0.4160	2
J1048+7143	S51044+71		bzq	1.15	7	J0721+7120	S50716+71	F12	bzb	0.31	51
J1058+5628	TXS1055+567		bzb	0.143	12	J0738+1742	PKS0735+17	F12	bzb	0.4240	11
J1203+6031	SBS1200+608		bzb	0.065	17	J0750+1231	OI280	F1	bzq	0.8890	11
J1248+5820	PG1246+586		bzb	0.8474	13	J0809+5218	1ES0806+524	TeV	bzb	0.1370	4
J1512-0905	PKS1510-08	F12	bzq	0.36	36	J0818+4222	S40814+42	F12	bzb	0.5300	10
J1542+6129	GB6J1542+6129	F2	bzb	0.117	31	J0830+2410	S30827+24	F1	bzq	0.9420	6
J1553+1256	PKS1551+130	F2	bzq	1.308	30	J0854+2006	OJ287	F12	bzb	0.306	26
J1555+1111	PG1553+113	F1	bzb	0.36	51	J0956+2515	OK290		bzq	0.7080	1
J1558+5625	TXS1557+565		bzb	0.3	34	J1012+0630	NRAO350		bzb	0.7270	1
J1604+5714	GB6J1604+5714		bzq	0.72	25	J1014+2301	4C23.24		bzq	0.5650	1
J1607+1551	4C15.54		bzb	0.496	25	J1018+3542	B21015+35B		bzq	1.2280	1
J1635+3808	4C38.41	F12	bzq	1.813	51	J1023+3948	4C40.25		bzq	1.2540	1
J1642+3948	3C345	F12	bzq	0.593	23	J1032+3738	B31029+378		bzb	0.5280	3
J1653+3945	Mkn501	F12	bzb	0.034	52	J1033+6051	S41030+61		bzq	1.4010	1
J1725+1152	1H1720+117		bzb	0.018	40	J1054+2210	87GB1051+2227		bzb	2.0550	1
J1748+7005	S41749+70		bzb	0.77	45	J1058+0133	4C1.28		bzb	0.8880	1
J1751+0939	OT81	F2	bzb	0.322	49	J1059-1134	PKSB1056-113		bzb	...	1
J1754+3212	BZBJ1754+3212		bzb	...	31	J1104+0730	GB6J1104+0730		bzb	0.6303	1
J1800+7828	S51803+784	F12	bzb	0.68	30	J1104+3812	Mkn421	F12	bzb	0.0300	3
J1806+6949	3C371	F1	bzb	0.05	39	J1121-0553	PKS1118-05		bzq	1.2970	1
J1809+2041	RXJ1809.3+2041		agu	...	28	J1132+0034	PKSB1130+008		bzb	0.6780	2
J1813+3144	B21811+31		bzb	0.117	27	J1159+2914	Ton599	F12	bzq	0.7250	1
J1836+3136	RXJ1836.2+3136		bzb	...	25	J1217+3007	1ES1215+303	TeV F2	bzb	0.1300	16
J1838+4802	GB6J1838+4802		bzb	0.3	28	J1220+0203	PKS1217+02		bzq	0.2404	1
J1841+3218	RXJ1841.7+3218		bzb	...	24	J1221+2813	WComae	TeV F12	bzb	0.1030	7
J1903+5540	TXS1902+556		bzb	...	27	J1221+3010	PG1218+304	TeV	bzb	0.1840	2
J1927+6117	S41926+61		bzb	...	25	J1222+0413	4C+04.42		bzq	0.9660	1
J1959+6508	1ES1959+650	F1	bzb	0.049	35	J1224+2122	4C21.35	TeV F1	bzq	0.4340	8
J2005+7752	S52007+77		bzb	0.342	27	J1224+2436	MS1221.8+2452	TeV	bzb	0.2180	5
J2015-0137	PKS2012-017		bzb	...	27	J1229+0203	3C273	F12	bzq	0.1580	1
J2016-0903	PMNJ2016-0903		bzb	...	22	J1230+2518	ON246		bzb	0.1350	1
J2022+7611	S52023+760		bzb	0.594	28	J1231+2847	B21229+29		bzb	0.2360	1
J2030-0622	TXS2027-065		bzq	0.671	26	J1238-1959	PMNJ1238-1959		agu	...	1
J2039-1046	TXS2036-109		bzb	...	32	J1245+5709	BZBJ1245+5709		bzb	1.5449	1
J2131-0915	RBS1752		bzb	0.449	28	J1253+5301	S41250+53		bzb	0.1780	2
J2143+1743	OX169	F2	bzq	0.211	29	J1256-0547	3C279	F12	bzq	0.5360	19
J2148+0657	4C6.69		bzq	0.999	29	J1314+2348	TXS1312+240		bzb	2.1450	1
J2149+0322	PKSB2147+031		bzb	...	23	J1337-1257	PKS1335-127		bzq	0.5390	1
J2150-1410	TXS2147-144		bzb	0.229	20	J1354-1041	PKS1352-104	F2	bzq	0.3320	1
J2202+4216	BLLacertae	F12	bzb	0.069	77	J1357+0128	BZBJ1357+0128		bzb	0.2187	2
J2225-0457	3C446	F1	bzq	1.404	22	J1427+2348	PKS1424+240	TeV	bzb	0.1600	7
J2232+1143	CTA102	F12	bzq	1.037	53	J1510-0543	PKS1508-05		bzq	1.1850	1
J2243+2021	RGBJ2243+203		bzb	...	32	J1512+0203	PKS1509+022		bzq	0.2190	1
J2251+4030	BZBJ2251+4030		bzb	0.229	33	J1516+1932	PKS1514+197		bzb	1.0700	1
J2253+1608	3C454.3	F12	bzq	0.859	103	J1548-2251	PMNJ1548-2251		bzb	0.1920	1
J2311+3425	B22308+34		bzq	1.817	30	J1550+0527	4C5.64		bzq	1.4170	2

Table 1 – *continued.*

ID (RBPL...)	Survey ID	Other[a]	Class[b]	z	N	ID (RBPL...)	Survey ID	Other[a]	Class[b]	z	N
J1608+1029	4C10.45		bzq	1.2320	2	J0825+6157	HB89-0821+621		RL-FSRQ	0.5420	8
J1637+4717	4C47.44		bzq	0.7350	3	J0854+5757	HB89-0850+581		RL-FSRQ	1.3191	6
J1640+3946	NRAO512		bzq	1.6660	1	J1551+5806	SBS1550+582		RL-FSRQ	1.3240	26
J1643-0646	FRBAJ1643-0646		bzb	...	1	J1603+5730	HB89-1602+576		RL-FSRQ	2.8580	15
J1649+5235	87GB1648+5240		bzb	2.055	30	J1624+5652	SBS1623+569	discontinued[c]	BL Lac	0.4150	18
J1722+1013	TXS1720+102		bzq	0.7320	1	J1638+5720	HB89-1637+574	discontinued[c]	RL-FS RQ	0.7506	24
J1727+4530	S41726+45		bzq	0.7140	1	J1800+3848	HB89-1758+388		RL-FSRQ	2.0920	16
J1733-1304	PKS1730-13	F12	bzq	0.9020	1	J1835+3241	3C382		...	0.0579	16
J1745-0753	TXS1742-078		bzb	...	1	J1854+7351	S5-1856+73		RL-FSRQ	0.4610	16
J1749+4321	B31747+433		bzb	0.2150	1	J1927+7358	HB89-1928+738		RL-FSRQ	0.3021	13
J1813+0615	TXS1811+062		bzb	...	2	J1955+5131	HB89-1954+513	new[d]	RL-FSRQ	1.2200	2
J1824+5651	4C56.27	F1	bzb	0.6640	2	J2016+1632	TXS2013+163		VisS	...	11
J1844+5709	TXS1843+571		agu	...	1	J2024+1718	GB6J2024+1718		RL-FSRQ	1.0500	13
J1848+3244	B21846+32B		agu	...	1	J2033+2146	4C+21.55	new[d]	QSO	0.1735	4
J1849+6705	S41849+67	F2	bzq	0.6570	1	J2042+7508	4C+74.26		QSO	0.1040	27
J1911-1908	PMNJ1911-1908		agu	...	1						
J1923-2104	TXS1920-211	F2	bzq	0.8740	1		*Not monitored GQ sources*				
J2000-1748	PKS1958-179		bzq	0.6520	1	J0702+8549	CGRaBSJ0702+8549		RL-FSRQ	1.0590	1
J2030+1936	87GB2028+1925		agu	...	1	J0728+5701	BZQJ0728+5701		RL-FSRQ	0.4260	2
J2031+1219	PKS2029+121		bzb	1.2130	1	J0837+5825	SBS0833+585		RL-FSRQ	2.1010	2
J2035+1056	PKS2032+107		bzq	0.6010	1	J1010+8250	8C1003+830		RL-FSRQ	0.3220	1
J2146-1525	PKS2143-156		bzq	0.6980	1	J1017+6116	TXS1013+615		RL-FSRQ	2.8000	2
J2147+0929	PKS2144+092	F2	bzq	1.1130	1	J1148+5924	NGC3894		B Lac-GD	0.0108	1
J2152+1734	S32150+17		bzb	0.8740	1	J1436+6336	GB6J1436+6336		RL-FSRQ	2.0680	1
J2217+2421	B22214+24B		bzb	0.5050	1	J1526+6650	BZQJ1526+6650		RL-FSRQ	3.0200	2
J2253+1404	BZBJ2253+1404		bzb	0.3270	1	J1623+6624	...		RL-FSRQ	0.201	2
J2321+2732	4C27.5		bzq	1.2530	1	J1727+5510	GB6J1727+5510		BL Lac-GD	0.2473	4
J2325+3957	B32322+396	F2	bzb	...	1	J1823+7938	S51826+79		BL Lac-GD	0.2240	4
						J1850+2825	TXS1848+283		RL-FSRQ	2.5600	3
	Monitored GQ sources					J1918+4937	BZQJ1918+4937		RL-FSRQ	0.9260	3
J0017+8135	...		RL-FSRQ	...	11	J1941-0211	PMNJ1941-0212		RL-FSRQ	0.2020	5
J0642+6758	HB89-0636+680		RL-FSRQ	3.1800	11	J2022+6136	S42021+61		RL-FSRQ	0.2270	6
						J2051+1742	PKS2049+175	Blazar	U	0.1950	3

[a]Indicates whether a source is part of another monitoring sample. 'TeV' marks sources that are in the TeV monitoring sample; 'F' marks sources of the F-GAMMA sample. The designation '1' tags F-GAMMA sources before and '2' those after F-GAMMA sample change/revision in middle 2009.
[b]Source classification. The tags 'bzq', 'bzb' and 'agu' are taken directly from the 2FGL. 'RL-FSRQ' stands for 'QSO RLoud flat radio sp', 'BL Lac – GD' stands for 'BL Lac – galaxy dominated', and 'Blazar U' stands for 'Blazar Uncertain type' of the Roma BZCAT – 5th edition (Massaro et al. 2015). Other designations have been taken from NASA/IPAC Extragalactic Database (NED).
[c]Discontinued after the completion of the second season.
[d]Introduced after the second season (2014) in exchange of the two sources that appeared in the 3FGL.

(iii) Central mask edge proximity, which may severely affect the photometry.

All the data products discussed here are based on data sets that have passed all these checks.

3 DATA PRODUCTS

In this section, we present minimal-processing data products for all sources included in Table 1.

Table 2 lists polarimetry and photometry data products for the sources observed. For polarization angles, we adopt the IAU convention: the reference direction is north, and the angle increases eastwards (Saikia & Salter 1988). The table columns include the number of times N each source has been observed to be significantly polarized ($p/\sigma_p \geq 3$), the average time between two such consecutive measurements $\langle\tau\rangle$, the median polarization fraction $\hat{p}$, the minimum and maximum polarization fractions ever observed for each source ($p_{\rm min}$ and $p_{\rm max}$, respectively), a flag indicating whether the source is of 'high polarization' (HP) or 'low polarization' (LP, with HP indicating that the source has at some point been observed to have a polarization fraction higher than 0.03), and the median polarization angle, $\hat{\chi}$. Polarization angles have been corrected for instrumental rotation. The polarization fraction has not been corrected for the host galaxy contribution (see Appendix A) or the statistical bias (Wardle & Kronberg 1974). We consider that the maximum-likelihood data analysis, which we use (see Section 3.2), is automatically accounting for the statistical bias since only statistically significant values of fractional polarization with ($p/\sigma_p \geq 3$) are used, for which the bias is negligible.

Concerning photometry data products, Table 2 lists the mean R-band magnitude for each source $\langle R\rangle$, averaged over all observations with significant photometry measurements, and the catalogue used for the photometry calibration.

3.1 Intrinsic mean flux density and modulation index

We have used the maximum-likelihood analysis presented in Richards et al. (2011) on the R-band flux densities in order to estimate the intrinsic mean flux density S_0 and its modulation index m_S, as well as uncertainties for these quantities. The analysis assumes that, discarding timing information, the underlying distribution of fluxes that the source is capable of producing is Gaussian.

Table 2. Observed polarization parameters and R-band magnitudes. $\hat{p}$ is the median polarization fraction and $\hat{\chi}$ the median polarization angle. For both quantities, only measurements that gave significant polarization degree ($p/\sigma_p \geq 3$) have been used. The angles are corrected for the instrumental rotation. $\langle R \rangle$ is the mean R-band magnitude. No extinction correction has been applied to these data.

		Raw polarization parameters						Raw photometric data	
ID (RBPL...)	N	$\langle\tau\rangle$ (d)	$\hat{p}$	$p_{\rm min}$	$p_{\rm max}$	Flag	$\hat{\chi}$ (°)	$\langle R \rangle$ (mag)	Photometry[a] catalogue
J0006−0623	10	39.2	0.249 ± 0.004	0.104 ± 0.013	0.355 ± 0.007	HP	−14.5	17.21 ± 0.02	ST
J0035+5950	4	14.3	0.033 ± 0.004	0.024 ± 0.008	0.049 ± 0.011	HP	81.3	17.62 ± 0.03	R2
J0045+2127	22	20.1	0.078 ± 0.001	0.036 ± 0.010	0.106 ± 0.007	HP	−86.7	16.64 ± 0.01	ST
J0102+5824	14	18.1	0.156 ± 0.004	0.058 ± 0.017	0.700 ± 0.104	HP	−82.2	17.95 ± 0.03	R2
J0114+1325	20	23.9	0.066 ± 0.001	0.027 ± 0.006	0.148 ± 0.006	HP	−67.0	16.15 ± 0.01	PTF
...	...	...	...	...	...	...	...	...	...

[a]Label indicating the catalogue used for the absolute photometry calibration. 'R2' is used for USNO-B1.0 R2 (Monet et al. 2003); 'PTF' for PTF (Ofek et al. 2012); 'R1' for the USNOB1.0 R1 catalogue and 'ST' for photometry based on Landessternwarte Heidelberg-Königstuhl charts.

Table 3. Photometry and polarization maximum-likelihood analysis results. S_0 is the intrinsic mean R-band flux density and m_S its intrinsic modulation index; p_0 the mean intrinsic polarization fraction and $m_{\rm p}$ its intrinsic modulation index.

	Maximum-likelihood photometry			Maximum-likelihood polarization		
ID (RBPL...)	S_0 (mJy)	m_S	N	p_0	$m_{\rm p}$	N
J0006−0623	$0.448^{+0.026}_{-0.026}$	$0.175^{+0.055}_{-0.037}$	11	$0.223^{+0.035}_{-0.032}$	$0.449^{+0.127}_{-0.091}$	11
J0017+8135	$1.169^{+0.017}_{-0.019}$	$0.039^{+0.016}_{-0.010}$	11	–	–	–
J0035+5950	–	–	1	$0.031^{+0.004}_{-0.005}$	<0.642	5
J0045+2127	$0.746^{+0.014}_{-0.014}$	$0.087^{+0.016}_{-0.012}$	23	$0.074^{+0.004}_{-0.004}$	$0.288^{+0.059}_{-0.048}$	23
J0102+5824	$0.194^{+0.021}_{-0.020}$	$0.340^{+0.103}_{-0.068}$	13	$0.159^{+0.028}_{-0.022}$	$0.520^{+0.133}_{-0.110}$	16
...	...	...	...	...	...	...

Observational uncertainties in R-band flux density measurements as well as finite sampling are explicitly accounted for. Table 3 summarizes the results of our analysis.

3.2 Intrinsic mean polarization and intrinsic modulation index

In a similar fashion, we have used a maximum-likelihood analysis to compute best-guess estimates of the average intrinsic polarization fraction p_0 and the intrinsic polarization fraction modulation index $m_{\rm p}$ (p-distribution standard deviation divided by p-distribution mean), as well as uncertainties for these quantities. Physically, p_0 and $m_{\rm p}$ correspond to the sample mean and sample modulation index that one would measure for a source using an infinite number of fair-sampling, zero-observational-error data points. For this analysis, we have used all measurements, regardless of the signal-to-noise ratio of the polarization fraction.

The details of the method are described in appendix A of Blinov et al. (2016a). The underlying assumptions are that (a) a single polarization fraction measurement from a source follows the Rice distribution (and, implicitly, that the Stokes parameters Q and U have Gaussian, approximately equal uncertainties); and (b) the values of the polarization fraction that a source can produce follow a Beta distribution (chosen because it is defined in a closed [0,1] interval, as is the polarization fraction):

$$\mathrm{PDF}(p;\alpha,\beta) = \frac{p^{\alpha-1}(1-p)^{\beta-1}}{B(\alpha,\beta)}. \quad (1)$$

If the parameters a, β of this distribution are known, the intrinsic mean and its modulation index are then given by

$$p_0 = \frac{\alpha}{\alpha+\beta} \quad (2)$$

and

$$m_{\rm p} = \frac{\sqrt{\mathrm{Var}}}{p_0} = \frac{\alpha+\beta}{\alpha}\cdot\sqrt{\frac{\alpha\beta}{(\alpha+\beta)^2(\alpha+\beta+1)}}, \quad (3)$$

with Var the variance of the distribution.

An essential advantage of this approach is that it provides estimates of both uncertainties and, when appropriate, upper limits. The method has been applied only in the cases with at least three data points out of which at least two had $p/\sigma_p \geq 3$. All the results of our analysis are shown in Table 3.

4 ANALYSIS

Our analysis is focused on the behaviour of the polarization fraction p and its variability for GL and GQ sources. We first examine the median polarization fraction $\hat{p}$ of each source computed from measurements with $p/\sigma_p \geq 3$. This quantity has the advantage that it is very straightforward to define and compute. However, it only characterizes sources during their stages of significant polarization, ignoring non-detections and the associated cycles of low polarization. For this reason, we also include a realistic analysis which accounts for limited sampling, measurement uncertainties, and Ricean bias, by applying a maximum-likelihood analysis to compute the intrinsic mean polarization fraction p_0 and its associated intrinsic modulation index $m_{\rm p}$ (Section 3.2), together with uncertainties for these quantities. A similar approach is followed for the photometry (Section 3.1), where a maximum-likelihood approach is used to compute the intrinsic mean R-band flux density S_0 and its intrinsic modulation index m_S. The scope of the section can be summarized as (a) quantifying the difference in the amount of polarization seen on average in GL and GQ sources and its variability, (b) searching

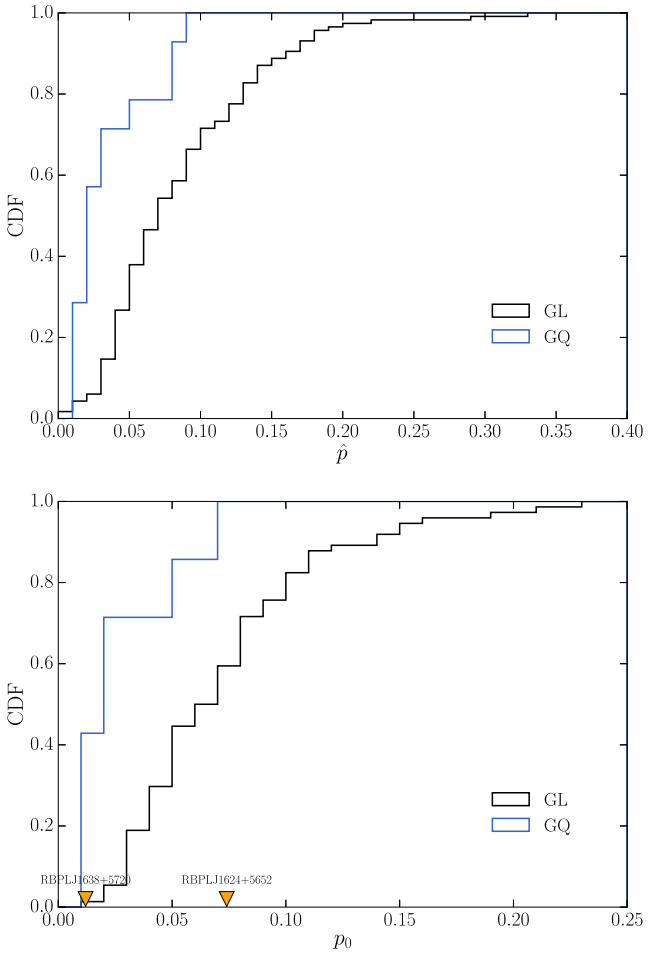

Figure 1. The cumulative distribution function of the median polarization fraction for the GL (black) and GQ samples (blue lines). Lower: same for the intrinsic polarization fraction p_0. The orange triangles indicate the sources that switched from the GQ sample to the GL in the 3FGL catalogue.

for parameters they may depend on, and (c) investigating the possible scenarios that would explain that difference.

4.1 The polarization of the GL and GQ samples

On the basis of mostly single-measurement data sets collected during the instrument commissioning phase around 2013 May–July, we showed that the polarization fraction of the GL and GQ targets cannot be drawn from the same parent distributions (see Survey Paper). Assuming an exponential distribution for both classes, the mean values $\langle p \rangle$ were $6.4^{+0.9}_{-0.8} \times 10^{-2}$ for GL and $3.2^{+2.0}_{-1.1} \times 10^{-2}$ for GQ sources.

Here, we address the same questions using our monitoring data and in particular $\hat{p}$ and p_0 for each source. In the upper panel of Fig. 1, we show the cumulative distribution function for the median polarization fraction $\hat{p}$ of each source. The median is computed from measurements satisfying the condition $p/\sigma_p \geq 3$. That leaves 116 GL and 14 GQ sources. The median of median polarization fractions is found to be 0.074 ± 0.007 for the GL sample and 0.025 ± 0.009 for the GQ ones. The null hypothesis that the two samples come from the same distribution was tested with a two-sample Kolmogorov-Smirnov (K-S) test which obtained a D of 0.611 and p-value of less than 8×10^{-5} (more than 4σ significance).

Assuming that $\hat{p}$ follows a lognormal distribution for each sample

$$\mathrm{PDF} = \frac{1}{x\sigma\sqrt{2\pi}} \exp - \frac{(\ln x - \mu)^2}{2\sigma^2} \quad (4)$$

which would imply an arithmetic mean of

$$\langle p \rangle = \mathrm{e}^{\mu+\sigma^2/2} \quad (5)$$

and an arithmetic variance of

$$\mathrm{Var} = (\mathrm{e}^{\sigma^2} - 1)\mathrm{e}^{2\mu+\sigma^2}, \quad (6)$$

we obtain best-fitting parameters for the mean $\hat{p}$ and the standard error in the mean ($\sqrt{\mathrm{Var}/N}$ with N the sample length). These are 0.101 ± 0.007 for the GL and 0.035 ± 0.009 for the GQ samples, respectively.

In the lower panel of Fig. 1, we repeat the exercise using the intrinsic polarization fraction p_0 described in Section 3.2. There we show 74 GL and 7 GQ sources for which reliable estimates of p_0 have been obtained. The median $\hat{p_0}$ for the two samples is 0.071 ± 0.006 and 0.020 ± 0.011, respectively. A two-sample K-S test gave a p-value of $\sim 2 \times 10^{-3}$. A major advantage of the maximum-likelihood method is that it provides upper limits. We repeated the previous analysis including the three GL and the one GQ source for which only 2σ upper limits on p_0 were available. We used the non-parametric two-sample tests in the ASURV package (Lavalley, Isobe & Feigelson 1992), suitable for censored data, to estimate the probability that the two distributions come from the same population. According to Gehan's generalized Wilcoxon test, the p-value is 10^{-3} indicating the persistence of the difference between the GL and GQ samples. Assuming again that the two samples are best described by a lognormal distribution and after including the 2σ upper limits, the mean intrinsic polarization of the sample $\langle p_0 \rangle$ is 0.092 ± 0.008 for GL and 0.031 ± 0.008 for GQ sources. These are the values that we consider the best guess to characterize the two source groups.

To examine whether the observed separation is affected by the class of GL sources, we compared the GQ sample separately with the GL BL Lac objects (sample 'GL-b') and GL flat-spectrum radio quasars (FSRQs, sample 'GL-q'). Using $\hat{p}$ which is available for larger samples, we find that the significance of the separation remains in the case of GL-b above the 4σ level while for the GL-q it is around 2.8σ. We consider the limited size of the latter sample the reason for the lower significance.

To summarize, based on either $\hat{p}$ or p_0, GL are on average significantly more polarized than GQ blazars, and this is not an artefact of different source classes dominating the GL and GQ sample. In the following sections, we investigate whether this dichotomy can be explained in terms of a dependence on the redshift, luminosity, the synchrotron peak frequency, colour, and source variability.

4.2 Polarization fraction and redshift

In this section, we examine whether $\hat{p}$ shows any dependence on the source redshift, z, and whether the redshift distribution of the members of the GL and GQ samples could be one of the factors responsible for the different degree of polarization of GL and GQ sources.

In Fig. 2, we show the redshift distribution of the GL and GQ sources of our sample. There we adopt the Roma-BZCAT[1] source designation (Massaro et al. 2015): 'bzb' for BL Lac objects (i.e.

[1] https://heasarc.gsfc.nasa.gov/W3Browse/all/romabzcat.html

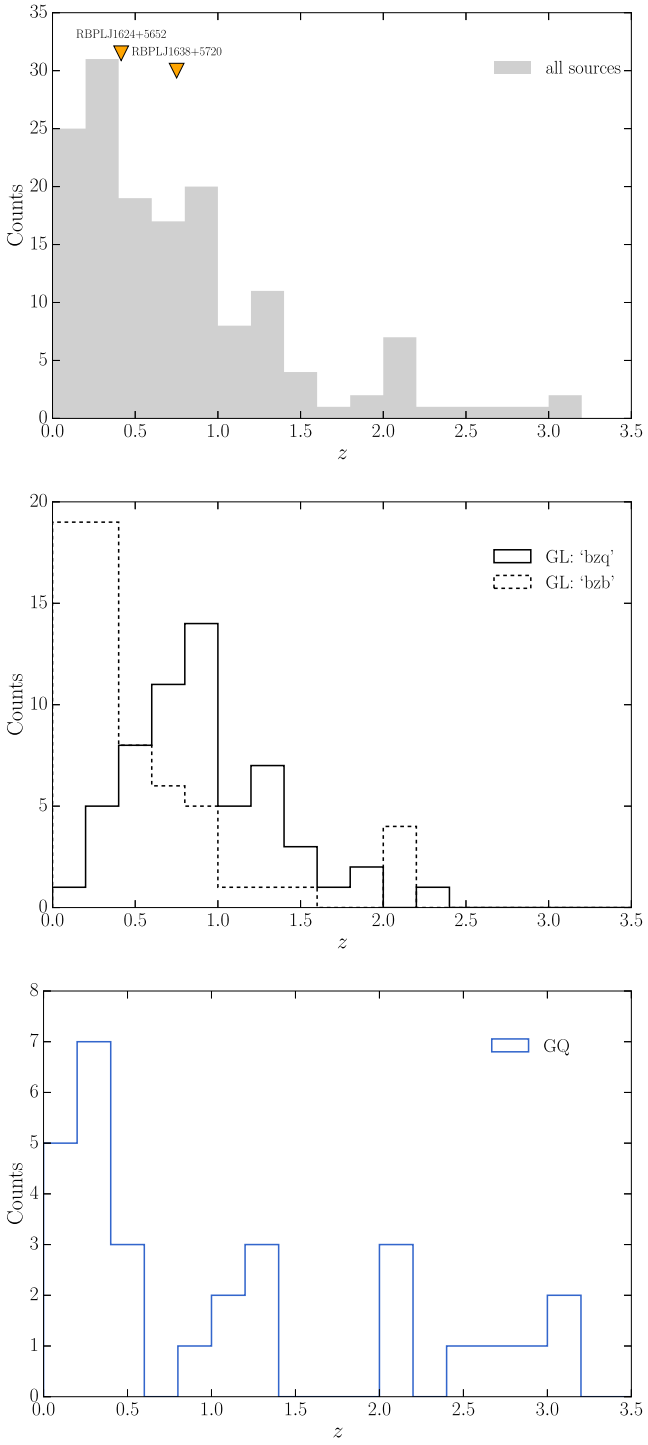

Figure 2. The redshift distribution of the main source classes in Table 1. The bin size is set to 0.2. Top panel: the grey area shows the distribution of all sources in Table 1. The orange triangles show the redshifts of the two sources which were initially selected as control sample sources but eventually appeared in the 3FGL list. Middle panel: the GL subset is shown separately for 'bzq' and 'bzb' sources following the 2FGL classification. Bottom panel: the GQ sources (control sample) are shown in blue.

AGNs with a featureless optical spectrum, or having only absorption lines of galaxian origin and weak and narrow emission lines), and 'bzq' for FSRQs (with optical spectrum showing broad emission lines and dominant blazar characteristics). GL sources classified as

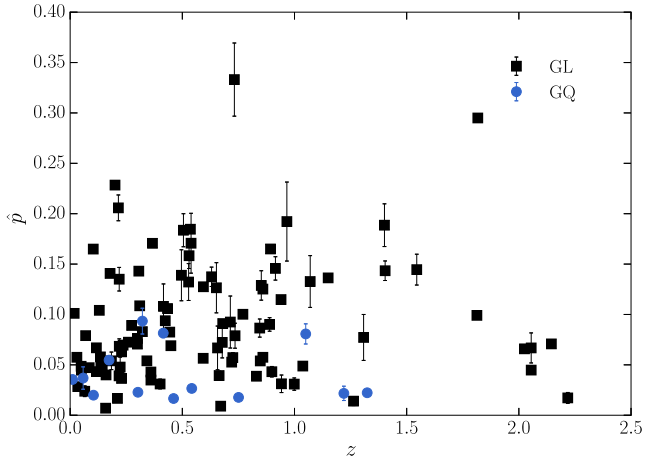

Figure 3. The median polarization fraction versus the source redshift for GL and GQ sources. The plot shows no evidence for a monotonic correlation.

'bzb' are found at systematically lower redshifts (median 0.308) as opposed to 'bzq' sources that have a higher median redshift of 0.867, as systematic studies of blazar samples have shown (e.g. Massaro et al. 2009). The GQ sources on the other hand are almost uniformly distributed over a broad range of redshifts reaching up to 3.18. Hence, their cosmological distance cannot explain – at least not alone – their gamma-ray silence. Their median redshift is around 0.5. The orange triangles mark the positions of the two GQ that appeared in the 3FGL (Acero et al. 2015).

The fact that the quasar subset of blazars (FSRQs) are observed at larger redshifts can impose a mild dependence of the population admixture on redshift (fig. 2 in Massaro et al. 2009 and fig. 1 in Xiong et al. 2015). If at the same time the degree of polarization depended on the source class (FSRQ or BL Lac), one could expect an implicit dependence of the polarization fraction on the redshift. Furthermore, the apparent dominance of quasars in the GQ sample (Table 1) would impose a similar dichotomy between GL and GQ samples.

As we discuss in Section 4.3, the contamination of the *R*-band emission by a big blue bump (BBB) component of thermal origin may modify the intrinsic polarization fraction of a source (e.g. Smith, Allen & Angel 1993). For quasars that are observed at higher cosmological distances, this may become significant. The imbalance of the two main source classes in our samples could naturally introduce artificial dichotomies. To rule out this possibility, we examined the population polarization parameters for the GL-b and GL-q samples. We found that (a) the two distributions are indistinguishable (K-S test p-value: 0.343), and (b) the mean polarization fraction for the GL-b is 0.087 ± 0.005 and for the GL-q 0.098 ± 0.012. This excludes the source class as the possible reason for the detected GL–GQ dichotomy.

Fig. 3 shows $\hat{p}$ versus z separately for the GL and GQ samples. In order to test whether $\hat{p}$ depends on z, we calculated the Spearman's rank correlation coefficient, ρ. The method assesses the possibility for the existence of a relation between the variables in the form of a monotonic function. Generally, ρ takes the value of -1 or $+1$ in the ideal case of a monotonic relation between the two variables and 0 in the total absence of such a relation. The case of $\hat{p}$ and z gives a ρ of only 0.18 (p-value: 0.065), lending no support to the hypothesis that there is significant correlation between the two. The same conclusion is reached when using the intrinsic mean polarization fraction p_0. However, Spearman's test evaluates only

the likelihood of a monotonic relation between two variables, so a more complicated relation cannot be excluded.

Since no strong correlation between redshift and polarization fraction has been identified, we find no indication that a difference in the redshift distribution between GL and GQ samples can be the source of their polarization dichotomy.

4.3 Polarization fraction and luminosity

Motivated by the deficiency of apparently bright and highly polarized sources reported in the Survey Paper (see fig. 3 therein), we examine the dependence of the source polarization on its *R*-band optical luminosity density, *L*, and whether such a dependence may be the source of the polarization dichotomy we have identified between GL and GQ sources.

In the Survey Paper, we proposed two alternative explanations for the observed deficiency: (a) the host galaxy unpolarized starlight contribution (e.g. Andruchow, Cellone & Romero 2008) and (b) the dust-induced polarization (e.g. Andersson, Lazarian & Vaillancourt 2015; Panopoulou et al. 2015) even though at rather low levels (∼1 per cent). In the case of AGN blazars, this effect must be insignificant as AGNs are generally hosted by dust-poor elliptical galaxies (Nilsson et al. 2003) although not exclusively (van Dokkum & Franx 1995).

A third factor that could potentially contaminate the observed emission is that from a BBB (e.g. Smith et al. 1993). Depending on its relative intensity, it can contribute unpolarized emission that may modify the observed polarization fraction. Especially, for quasars this contribution can be significant and can comprise a considerable fraction of the emission observed in the *R* band. Under these circumstances, the observed emission cannot be attributed purely to the jet – which is our implicit assumption – but at least partly to the BBB, as well.

A way around the problem would be to compare jet luminosities, a non-trivial task. Instead, we chose to investigate the likelihood that our sample suffers from this effect. For 104 sources in Table 1, Spectral Energy Distributions (SEDs) are available from Mao et al. (2016). Only 15 of these sources (∼14 per cent) showed a clear signature of a BBB, 69 (∼66 per cent) do not have a significant contribution of a BBB, and for 20 sources the evidence for a BBB is inconclusive. Consequently, the possibility that our findings are influenced by the contribution of a BBB is negligible. We emphasize that even in the cases with clear contributions of a BBB, the amount of contamination depends on the relative intensity. We conclude that although the BBB must always be taken into account, its potential contribution to the total intensity in a small fraction of the RoboPol sources does not affect our results.

In Fig. 4, we show the median polarization fraction $\hat{p}$ as a function of the rest-frame spectral luminosity for sources in the GL and GQ samples. As we explain in Appendix A, the luminosity coordinate has been subjected to (a) galactic extinction correction (using extinction values from the NASA/IPAC Extragalactic Database, NED), (b) host galaxy contribution removal (see Appendix A), and (c) *K*-correction assuming a spectral index of $\alpha = -1.3$ for an optical SED following a power law of the form ν^{α} (Fiorucci, Ciprini & Tosti 2004; Hovatta et al. 2014). In total, we show 82 GL and 14 GQ sources. For 32 GL sources, the host galaxy contribution has been removed (cf. Table A1). A Spearman's rank-order correlation coefficient computed for GL and GQ sources collectively gave a correlation index 0.028 (*p*-value: 0.752), showing no evidence for a monotonic relation. A similar result is found when the host galaxy contribution is removed from the polarization fraction.

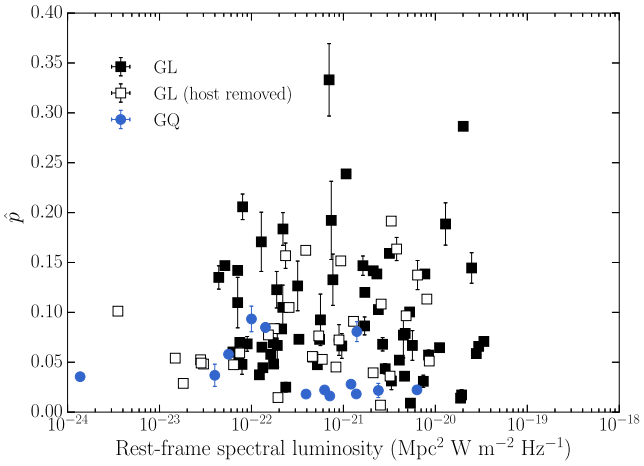

Figure 4. The median polarization fraction as a function of the *R*-band rest-frame spectral luminosity. We show separately the GL (82 squares) and GQ samples (14 circles). For 32 GL, the host contribution has been subtracted (open squares).

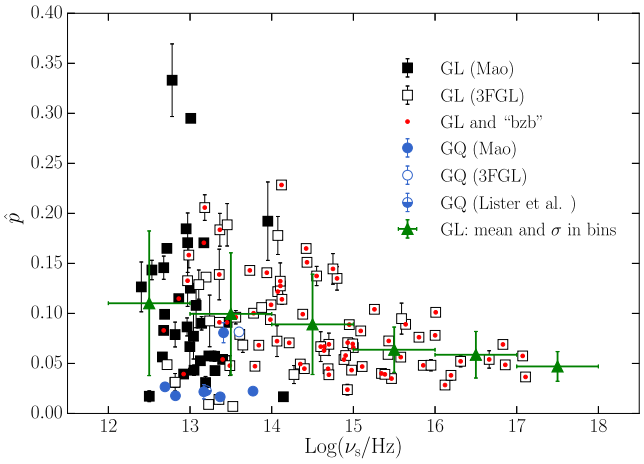

Figure 5. The polarization fraction as a function of the rest-frame synchrotron peak frequency. The squares mark GL sources and the circles GQ ones. For the filled symbols, the peak frequency was taken from Mao et al. (2016) while for the open ones from 3FGL or Lister et al. (2015). The red dots denote the BL Lac subset of GL sources. The green triangles correspond to the mean within each frequency bin. The bin width is marked with the *x*-axis error bar and has a total length of one. The *y*-axis error bars have a length of one standard deviation computed within the bin.

Therefore, there is no indication in our data that the GL–GQ polarization fraction dichotomy can be traced to a difference in jet luminosity at optical wavelengths between the two samples.

4.4 Polarization as a function of the synchrotron peak frequency

The location of the synchrotron peak may be another factor affecting the average polarization properties of the GL and GQ samples. To study such a possible effect, we plot, in Fig. 5, the median polarization fraction $\hat{p}$ against the logarithm of rest-frame synchrotron peak frequency for the GL and GQ sources.

The synchrotron peak frequencies – for both samples – were estimated through a second-order polynomial fit to the synchrotron peak of their SED using data presented in Mao et al. (2016). Their

data sets include two radio frequencies – at 1.4 (from NVSS and FIRST catalogues; White et al. 1997; Condon et al. 1998) and at 5 GHz from the GB6 and PMN catalogues (Wright et al. 1994; Gregory et al. 1996) – four infrared frequencies from *WISE*,[2] and four optical filters (z, i, r, g) from the SDSS DR9 (Ahn et al. 2012). The X-rays were extracted from the *Swift* archive (Burrows et al. 2005) and gamma-rays from the 3FGL (Acero et al. 2015). All fluxes were K-corrected to the rest frame before obtaining luminosities and the fitting was done in logarithmic luminosity space. Details of the data and the corrections applied to them are given in Mao et al. (2016). Although the SDSS u band has been excluded from our data set to avoid the influence of a possible BBB, such a contribution may still be present. For that reason, we inspected all our SEDs to identify problematic cases. Indeed, for 16 of the GL sources, we found that a BBB had or could have had an effect on the localization of the peak. For those cases, the synchrotron peak frequency was taken from the 3FGL (Ackermann et al. 2015), instead. For the GQ sample, three sources could have been affected by the presence of a BBB. For two of them, peak values were available from the 3FGL and Lister et al. (2015), while the third one was excluded. All the values used here are given in Table 4.

Fig. 5 shows the dependence of median polarization on synchrotron peak frequency. It can be seen there that there is an upper envelope that decreases with increasing synchrotron peak frequency. However, a Spearman test does not favour a significant monotonic anti-correlation. The anti-correlation strength is only $\rho = -0.2$ (p-value: 0.04), when calculated collectively for all GL and GQ sources. For the GL sources, however, the synchrotron-peak-frequency estimates are more reliable owing to the better and denser data sets available. Applying the test to the GL sources alone revealed some anti-correlation with a ρ around -0.3 and a p-value of 2×10^{-3}. If the test is further restricted to only the BL Lac subset of GL sources (classified as 'bzb') which happen to cover a larger range of peak frequencies, it yields a $\rho \approx -0.5$ and a p-value of 6×10^{-6}.

In Fig. 5, we also plot the mean $\hat{p}$ (*green* markers) in each bin. The abscissa error bars mark the bin extent while the ordinate error bars show the spread of the $\hat{p}$ within the bin (error bar size is 1 standard deviation). A linear fit to the bin gives a significant slope of -0.012 ± 0.001.

It is clear then that low-synchrotron-peaked (LSP) sources appear more polarized than high-synchrotron-peaked (HSP) ones (with LSP, if $\log(\nu_s) < 14$, ISP if $14 \leq \log(\nu_s) < 15$, and HSP if $\log(\nu_s) \geq 15$, respectively); at the same time, their polarization varies over a broader range. However, as GQ sources are preferentially LSPs, this trend cannot explain their systematically lower polarization compared to GL sources.

4.5 Polarization angle randomness as a function of the synchrotron peak frequency

The polarization parameters have a strong dependence on the properties of the magnetic field (e.g. uniformity). Given the relation between the polarization fraction and the synchrotron peak frequency discussed above, we examine how the peak frequency may be influencing the behaviour of the EVPA.

Fig. 6 demonstrates how well a uniform distribution describes the behaviour of the EVPA of each source as a function of the frequency of its synchrotron SED component peak. For every source,

[2] http://wise2.ipac.caltech.edu/docs/release/allwise/

Table 4. The logarithm of the rest-frame synchrotron peak frequencies.

ID (RBPL...)	$\log(\nu_S/\mathrm{Hz})$	ID (RBPL...)	$\log(\nu_S/\mathrm{Hz})$
GL from Mao et al. (2016)			
J0136+4751	13.0	J1224+2122	13.9
J0238+1636	12.9	J1224+2436	15.4
J0259+0747	12.7	J1229+0203	13.5
J0423−0120	12.7	J1230+2518	14.9
J0442−0017	13.0	J1231+2847	15.0
J0510+1800	13.1	J1238−1959	14.1
J0750+1231	13.1	J1245+5709	14.8
J0841+7053	12.5	J1248+5820	14.9
J0957+5522	13.0	J1253+5301	13.9
J0958+6533	13.2	J1314+2348	14.9
J1159+2914	13.3	J1357+0128	14.8
J1222+0413	14.0	J1427+2348	15.3
J1256−0547	13.0	J1512+0203	13.6
J1337−1257	13.0	J1516+1932	13.0
J1512−0905	13.3	J1542+6129	14.6
J1553+1256	13.0	J1555+1111	15.5
J1604+5714	13.1	J1558+5625	14.2
J1635+3808	12.7	J1607+1551	13.4
J1637+4717	12.8	J1649+5235	14.4
J1642+3948	12.7	J1653+3945	16.1
J1722+1013	12.8	J1725+1152	16.0
J1751+0939	12.7	J1727+4530	13.2
J1800+7828	13.5	J1748+7005	13.8
J1824+5651	12.9	J1749+4321	13.2
J1849+6705	13.0	J1754+3212	14.3
J2000−1748	12.4	J1806+6949	14.7
J2005+7752	13.4	J1809+2041	15.4
J2143+1743	14.1	J1813+0615	14.1
J2148+0657	13.2	J1813+3144	15.0
J2225−0457	12.5	J1836+3136	14.9
J2253+1608	13.2	J1838+4802	15.8
J2311+3425	13.0	J1841+3218	16.3
J2334+0736	12.8	J1844+5709	14.3
		J1903+5540	14.4
GL from 3FGL		J1911−1908	15.9
J0045+2127	16.0	J1927+6117	13.4
J0114+1325	15.0	J1959+6508	16.9
J0136+3905	16.2	J2015−0137	14.4
J0211+1051	14.1	J2022+7611	14.1
J0217+0837	13.8	J2030−0622	13.2
J0222+4302	15.1	J2030+1936	15.6
J0303−2407	15.4	J2039−1046	13.8
J0336+3218	13.4	J2131−0915	16.8
J0339−0146	13.1	J2149+0322	14.1
J0340−2119	13.5	J2150−1410	17.1
J0721+7120	14.0	J2202+4216	13.6
J0738+1742	14.0	J2217+2421	13.4
J0809+5218	15.9	J2232+1143	12.7
J0818+4222	13.0	J2243+2021	15.6
J0830+2410	12.8	J2251+4030	14.6
J0848+6606	14.7	J2340+8015	15.6
J0854+2006	13.7		
J1032+3738	14.1	*GQ from Mao et al. (2016)*	
J1033+6051	13.5	J0825+6157	12.7
J1037+5711	14.7	J1551+5806	13.8
J1048+7143	13.2	J1638+5720	12.8
J1054+2210	14.6	J1854+7351	13.4
J1058+5628	15.1	J1955+5131	13.2
J1059−1134	13.6	J2024+1718	13.4
J1104+0730	14.6		
J1104+3812	17.1	*GQ from 3FGL*	
J1132+0034	14.1	J1624+5652	13.6
J1203+6031	14.9		
J1217+3007	15.3	*GQ from Lister et al. (2015)*	
J1221+2813	14.4	J1927+7358	13.2
J1221+3010	16.7		

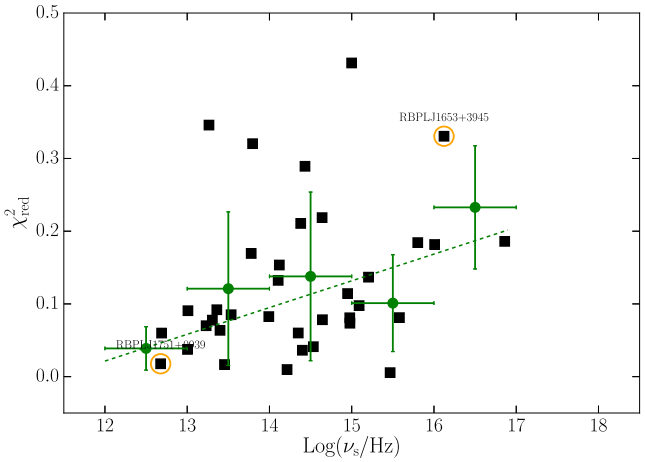

Figure 6. The randomness of EVPA as a function of the logarithm of the synchrotron peak frequency. The *y*-axis is the reduced χ^2 of the comparison of the source angle distribution with a uniform one. The green filled circles mark the average $\chi^2_{\rm red}$ in five bins. Their *x*-axis error bars have a length of half a bin width, while the *y*-axis mark the spread of $\chi^2_{\rm red}$ (one standard deviation) within that bin. The green dashed line is the best fit to the binned data (green points). The orange circles mark one case of high randomness of the EVPA (i.e. close to uniform), RBPLJ1751+0939, and one case with low randomness (i.e. far from uniform), RBPLJ1653+3945. The angle distributions of these two cases are shown in Fig. 7.

we compute the χ^2 per degree of freedom, $\chi^2_{\rm red}$, between its angle distribution and a uniform one. The computation has been done for 36 sources for which at least 20 measurements with $p/\sigma_p \geq 3$ are available so that a reliable estimate of the angle randomness can be provided. Our calculations are done for 20 angle bins in the closed $[-90, +90]$ interval. A large value of $\chi^2_{\rm red}$ implies a big divergence from a uniform distribution and hence a low randomness of the EVPA, which consequently centres around a preferred direction (e.g. Fig. 7, right-hand column). The opposite is the case for small $\chi^2_{\rm red}$ values which imply a large randomness of the EVPA that does not prefer any direction (e.g. Fig. 7, left-hand column). The orange circles in Fig. 6 mark the two exemplary cases shown in Fig. 7.

The Spearman's test does not support the presence of a monotonic relation between the EVPA randomness and the synchrotron peak frequency ($\rho = 0.34$, with a *p*-value $\sim$0.044). Two further tests, though, indicate a dependence between the two parameters.

First, we classified our 36 sources as low-, intermediate-, and high-synchrotron-peaked (LSP, ISP, and HSP, respectively). Then we selected 0.1 as the limiting value of $\chi^2_{\rm red}$ for a source to be considered as non-uniform. We then found that 11/14 (79 per cent) LSP, 7/14 (50 per cent) ISP, and 3/8 (38 per cent) HSP sources have $\chi^2_{\rm red}$ below 0.1. Despite the small number statistics, this result indicates that HSP sources are more likely to have a preferred and less variable EVPA than LSP sources.

Secondly, the *green* markers in Fig. 6 show the mean $\chi^2_{\rm red}$ in each of five synchrotron-peak frequency bins. The vertical error bars show the spread of the values in the bin (1σ). A linear fit to the binned data – the *green* dashed line – gives a significant slope of 0.037 ± 0.010.

We conclude that the randomness of the EVPA depends on the synchrotron peak frequency. The EVPA of HSP sources is concentrated around preferred directions. The EVPA of LSP sources, on the other hand, is more variable and less likely to have a preferred direction. In Section 5, we argue that these two findings may be evidence for a helical structure of the magnetic field.

4.6 Polarization and source variability

Depending on the mechanism producing the variability, it is likely that the degree of polarization relates to the degree of variability at different bands. Here we examine the role that the radio and the optical modulation indices may play.

In Fig. 8, we plot the median polarization fraction versus the variability amplitude at 15 GHz from Richards et al. (2014), as that is quantified through the intrinsic modulation index introduced by Richards et al. (2011). As shown there, the two are correlated with Spearman's test giving a $\rho \sim 0.35$ and a *p*-value of about 3×10^{-4}. The GQ sources have preferentially low radio modulation indices, as was already found by Richards et al. (2011). However, the GQ sources have average polarization fractions that are low even compared to GL sources with comparable radio modulation indices.

In Fig. 9, we examine the dependence of the polarization fraction on the variability amplitude of the *R*-band flux density. In the upper panel, we plot the observed median polarization fraction $\hat{p}$ and the *R*-band flux density modulation index m_S. In this case, Spearman's ρ, when including both GL and GQ sources, is around 0.38 with a *p*-value of 10^{-4}, indicating a rather significant correlation. Similarly, in the lower panel, we show the maximum-likelihood intrinsic mean polarization fraction p_0 and the m_S which gave a Spearman's $\rho \approx 0.38$ with a *p*-value of 8×10^{-4}. Again, GQ sources are systematically less polarized on average than sources with comparable optical modulation indices.

Finally, in Fig. 10, we examine whether p_0 depends on the amplitude of the variability quantified through the intrinsic polarization modulation index $m_{\rm p}$. Spearman's test gave a ρ of around -0.31 with a significance of *p*-value 0.013.

We conclude that the variability amplitude, in both radio and optical flux density, affects the mean observed polarization. With comparable Spearman's test results, higher polarization is associated with stronger variability in either the optical or the radio. Finally, there is also a weak indication that stronger variability in optical polarization associates (on average) with lower polarization although of lower significance. Nevertheless, these correlations cannot explain GL–GQ polarization dichotomy.

4.7 The polarization variability of the GL and GQ samples

Intrigued by the dichotomy between GL and GQ samples in terms of their polarization fraction and given the correlation between the $\hat{p}$ and the *R*-band modulation index (Fig. 9), we have searched for a similar dichotomy in the distribution of their polarization variability. We also consider its dependence of redshift.

The distribution of the intrinsic modulation index $m_{\rm p}$ is shown in Fig. 11 (77 GL and 8 GQ sources). Of these, 13 GL and 6 GQ sources having only 2σ upper limits were available. A standard two-sample K-S test could not distinguish the two distributions ($D = 0.36$ and *p*-value of 0.255). A Gehan's generalized Wilcoxon test indicated a similar result with a *p*-value of 0.167.

Contrary to the median polarization fraction $\hat{p}$ (see Section 4.2), the intrinsic modulation index $m_{\rm p}$ depends on the source redshift. In Fig. 12, the arrows indicate 2σ upper limits. A Spearman test for collectively the GL and the GQ sources, excluding the upper limits, gave a ρ of 0.43 and a *p*-value of 10^{-3}. When the upper limits are

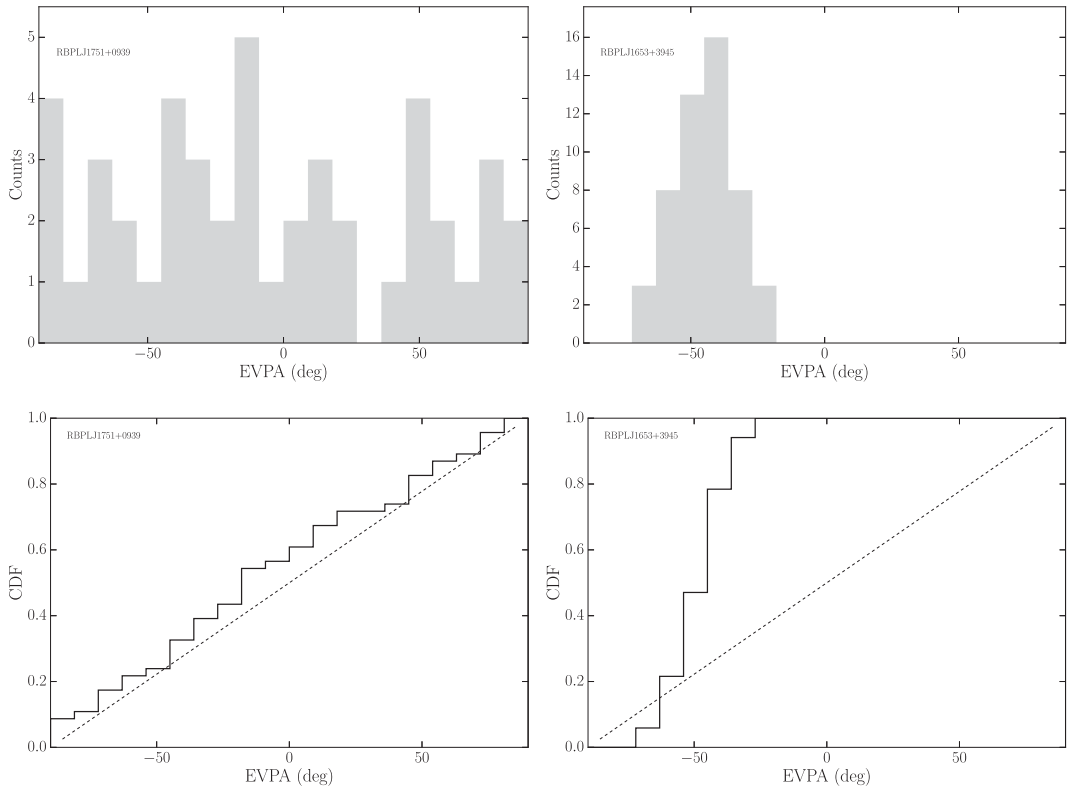

Figure 7. The distribution of EVPA for a close-to-uniform case (highly random, RBPLJ1653+3945, left) and one case far-from-uniform (low randomness, RBPLJ1751+0939, right). Upper row: the distribution of EVPA. Lower row: the cumulative distribution function of the EVPA for those two cases (solid line) and the one of uniform distribution (dashed line). There are 46 data angle measurements for RBPLJ1751+0939 and 51 for RBPLJ1653+3945.

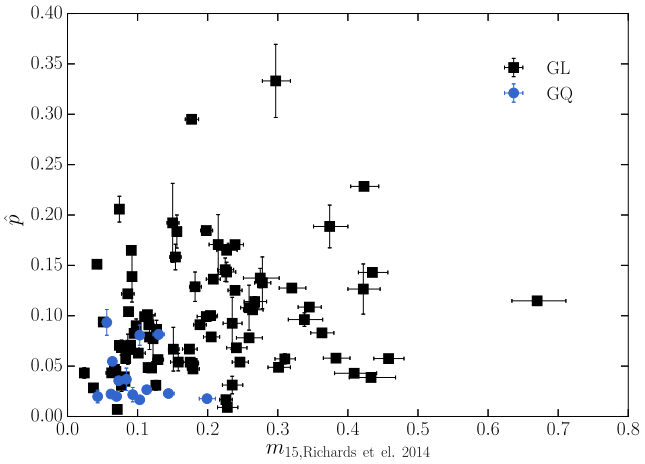

Figure 8. The median polarization fraction versus the 15 GHz intrinsic modulation index. In total, we show 86 GL and 14 GQ sources.

included (10 GL and 6 GQ sources), the correlation remains as tight ($\rho \approx 0.42$) but the significance improves by almost one order of magnitude with a p-value of 2×10^{-4}.

We conclude that although there is no dichotomy between the polarization variability index m_p of GL and GQ sources similar to the one seen for $\hat{p}$, a significant correlation exists between m_p and redshift.

4.8 Variability of optical flux density and polarization against the variability in other bands

We are now interested in examining whether the variability in the R band, both in total flux density and in fractional polarization, correlates with the variability in other bands. That would be expected in the radio and the optical if photons in those bands belong to the same synchrotron component.

For a total of 61 GL and 18 GQ sources, estimates for both m_{15} (Richards et al. 2014) and m_S are available. Those are shown in Fig. 13, and as it appears they are not correlated (Spearman's $\rho \approx 0.25$ with p-value 0.025).

Fig. 14 shows the intrinsic polarization modulation index m_p versus m_{15}. Whenever possible, 2σ upper limits are also shown. As in the m_{15}–m_S case, there is no clear correlation, implying that the amplitude of the 15 GHz total intensity variability is not connected to the variability amplitude of the optical polarization fraction. The validity of this conclusion, of course, relies on the assumption that the radio and optical data sets used carry the characteristics of the variability mechanisms even though they are not contemporaneous.

There is a weak indication of a possible mild correlation between the intrinsic polarization variability index m_p and the flux density variability index m_S, see Fig. 15. Using the GL sources alone gave a ρ around 0.3 although with a significance below the 2.5σ level (p-value ≈ 0.016).

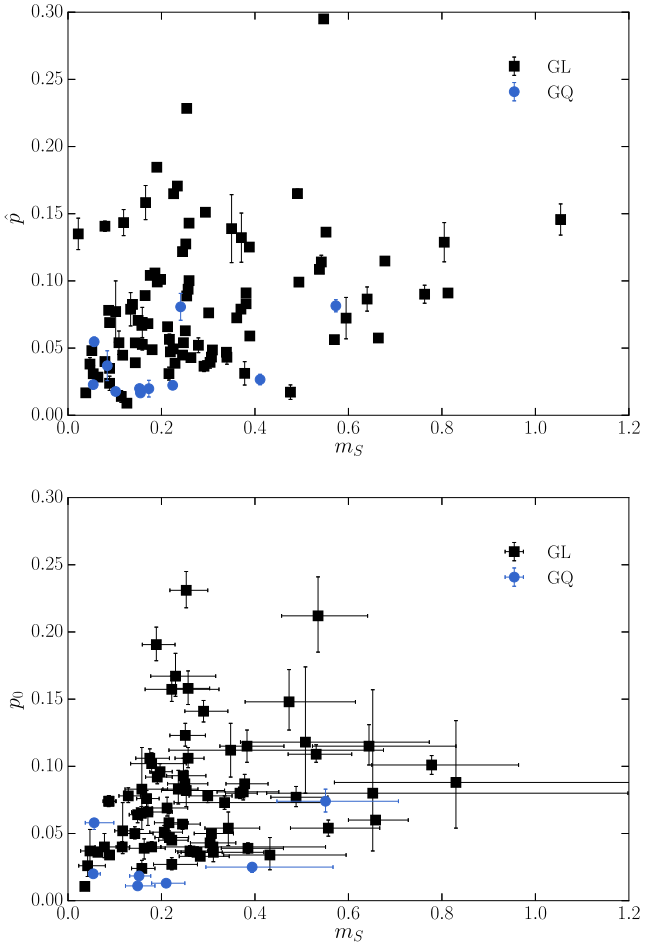

Figure 9. The polarization fraction versus the *R*-band flux density modulation index. The upper panel is using the median polarization fraction $\hat{p}$ and the lower one the intrinsic mean p_0.

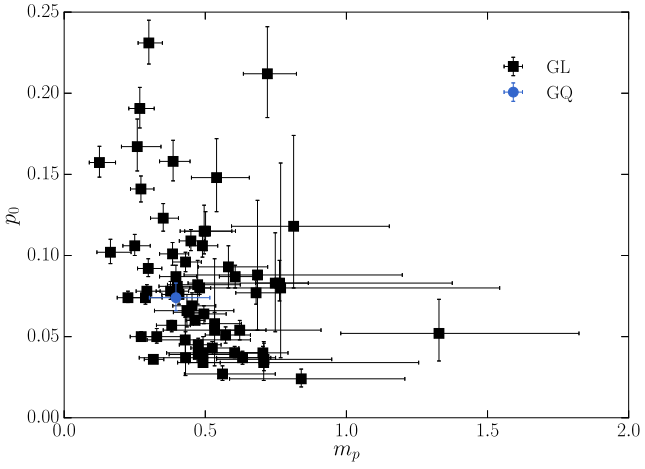

Figure 10. The mean intrinsic polarization fraction versus the intrinsic polarization modulation index.

5 SUMMARY AND DISCUSSION

We have presented the average polarimetric and photometric properties and the variability parameters, of GL and GQ sources observed with RoboPol during the first two observing seasons. Our analysis concentrated on (a) quantifying the possible difference in the

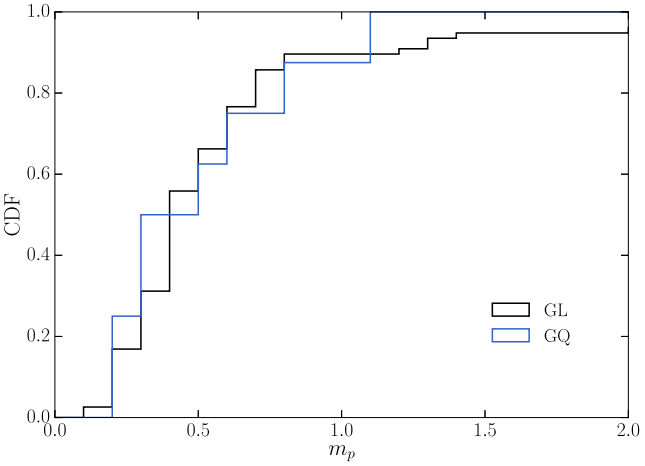

Figure 11. The intrinsic modulation index $m_{\rm p}$ for the GL and GQ samples. In the cases where the $m_{\rm p}$ was not available, 2σ upper limits have been included instead.

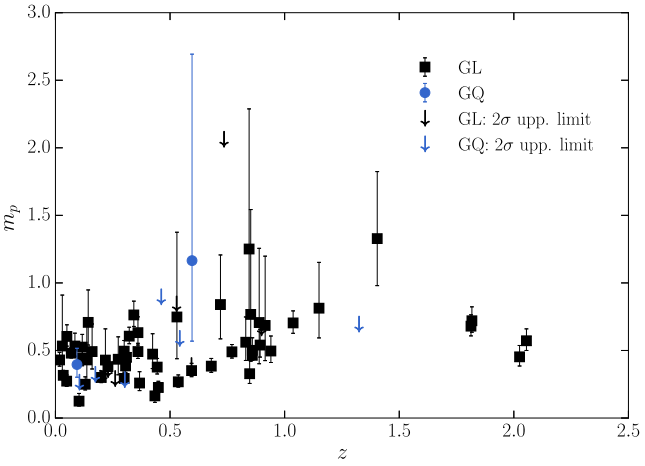

Figure 12. The intrinsic modulation index of the polarization fraction versus the redshift. The arrows indicate 2σ upper limits. The *y*-axis has been truncated at 3 excluding three GL upper limits close to 3.5, 4, and 7.

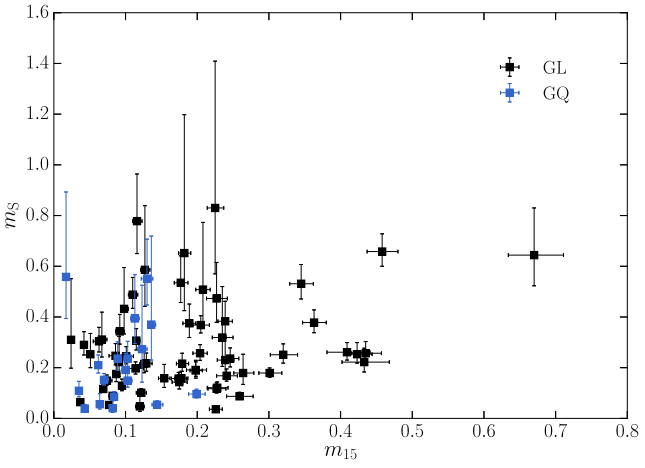

Figure 13. The *R*-band intrinsic modulation index m_S versus that at 15 GHz, m_{15}.

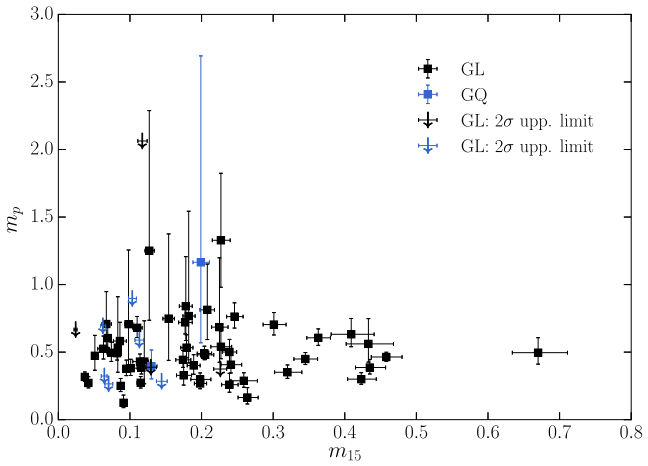

Figure 14. The intrinsic polarization modulation index $m_{\rm p}$ versus that at 15 GHz, m_{15}. The arrows mark 2σ upper limits. The y-axis is truncated at 3 excluding one upper limit around 7.

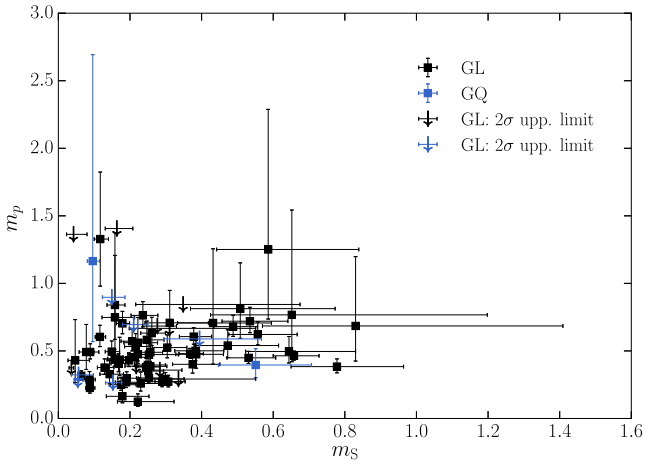

Figure 15. The median polarization fraction versus the modulation index of the R-band flux density, m_S. The y-axis has been truncated at 3 excluding three upper limits at around 3.5, 4, and 7.

polarization of the GL and GQ sources that was first found by Pavlidou et al. (2014); and (b) investigating its possible causes. We also examined whether the polarization variability shows a similar dichotomy for GL and GQ sources. We have found that the following.

The average polarization does not depend on luminosity. While in the Survey Paper the unpolarized starlight contribution of the host galaxy was suggested as being possibly responsible for the apparent de-polarization of the brightest sources, a more detailed analysis in luminosity space revealed that sources that are both very luminous and highly polarized are possible (see Fig. 4).

The average polarization fraction of GL and GQ sources differs. The two samples have different mean polarization fractions: the distributions of $\hat{p}$ are different at an almost 4σ level, while those of the intrinsic mean polarization fraction p_0 have yielded a significance of $\sim 3\sigma$. A Gehan's generalized Wilcoxon test applied on a data set including 2σ upper limits in p_0 produces a similar result (Fig. 1, lower panel). A lognormal distribution fit to the two distributions of p_0 gives the mean intrinsic polarization $\langle p_0 \rangle$ of $(9.2 \pm 0.8) \times 10^{-2}$ for GL and $(3.1 \pm 0.8) \times 10^{-2}$ for GQ sources.

The variability amplitude of the polarization fraction does not differ between GL and GQ sources. Unlike the polarization fraction, its variability amplitude does not show the same dichotomy between GL and GQ samples. However, the sample consisted of 64 GL and 2 GQ sources (of which 19 have only upper limits), so small number statistics may limit our ability to establish a difference between the two populations. This makes any conclusion concerning the distributions of $m_{\rm p}$ ambiguous. However, the very fact that for the majority of GQ sources we were able only to place upper limits on the amplitude of optical polarization variability may be seen as an indication that GQ sources are less variable. That is indeed the case in terms of radio and optical flux density modulation index as Figs 8 and 9 show.

The stronger the variability in radio or optical, the larger the mean polarization. Figs 8 and 9 suggest that the larger the amplitude of the radio and the R-band flux density variability, the higher is the median polarization. On the other hand, the polarization variability amplitude $m_{\rm p}$ does not seem to influence the median polarization, although there is even an indication that the two are anti-correlated (Fig. 10). We have also examined whether the high-energy (2FGL) variability index is influencing the polarization fraction and found no evidence for such a dependence.

The modulation index of the polarization fraction is redshift dependent. Contrary to the polarization fraction itself, its variability amplitude seems to be a function of redshift.

Source class is not the reason for the GL–GQ dichotomy. The dominance of radio quasars in the GQ sample could explain the observed dichotomy, if BL Lac objects and FSRQs were characterized by different distributions of p. A two-sample K-S test between quasars and BL Lac objects has shown that the two distributions are indistinguishable. It must be noted however that the GQ sources reach larger redshifts (Fig. 2) which could potentially have an effect on the gamma-ray detectability given the maximum redshift that *Fermi* can probe. Our findings however cannot be influenced by this; (a) because GQ sources for which $\hat{p}$-values are available and hence are included in our plots are limited to $z < 1.5$; and (b) as can be seen in Fig. 3, the degree of polarization is independent of the source cosmological distance.

The optical polarization fraction and the randomness of the polarization angle depend on the synchrotron peak frequency. Fig. 5 revealed a synchrotron-peak-dependent envelope limiting the polarization fraction: the fractional polarization $\hat{p}$ of LSP sources is on average higher than that for HSP ones, while their polarization spreads over a broader range extending to considerably higher values of $\hat{p}$. We have shown that if we exclude the GQ sources (for which the synchrotron peak is severely undersampled), there is a significant anti-correlation between $\hat{p}$ and the rest-frame frequency of the synchrotron peak, $\nu_{\rm s}$. The anti-correlation becomes clearer and more significant when only the 'bzb' subset of the GL sample is considered. A similar relation between the fractional polarization of the Very Long Baseline Array (VLBA) core and the synchrotron peak frequency has been found by Lister et al. (2011). When they have focused only on LSP and HSP BL Lac objects that span similar redshift ranges, they observe the

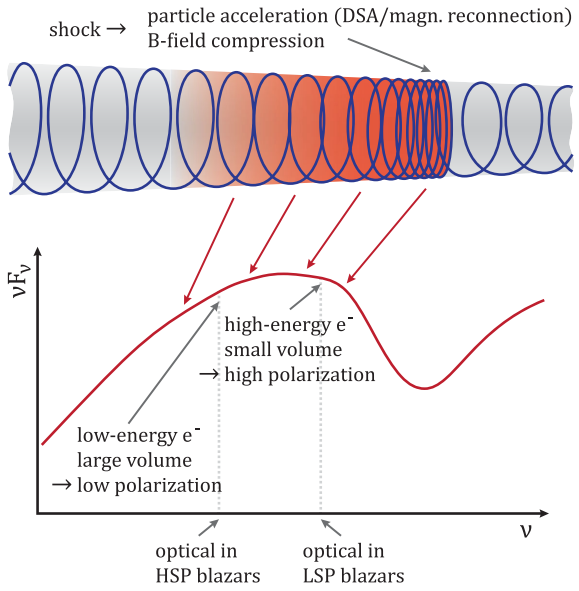

Figure 16. Cartoon representation of the shock-in-jet scenario. The downstream direction is towards the left.

same trend. They explain the observed correlation as a result of the balance between the intrinsic gamma-ray loudness and the Doppler boosting of the sources given the general association of high polarization to highly Doppler-boosted jets. Myserlis et al. (in preparation) look at the fractional polarization of roughly 35 *Fermi* sources and find that at 2.64 and 4.85 GHz the same relation is apparent. Specifically at 4.85 GHz they find that Spearman's $\rho = -0.35$.

We also show that apart from the polarization fraction, the randomness of the EVPA depends on the synchrotron peak frequency. LSP sources tend to show a random orientation of their, unlike HSP sources which tend to show a preferred direction.

5.1 A qualitative interpretation of the observed trends

In this section, we propose a simple, qualitative explanation for the various trends of the average degree of polarization found in this study. It is based on a basic shock-in-jet scenario, as sketched in Fig. 16. The jet is expected to be pervaded by a helical magnetic field structure, on which a turbulent B-field component is superposed. A mildly relativistic shock, caused either by a static disturbance in the environment of the jet (i.e. a standing shock) or by the collision of plasmoids propagating along the jet with different Lorentz factors (internal shock), mediates efficient particle acceleration due to diffusive shock acceleration or magnetic reconnection in a small volume, concentrated in the immediate downstream environment of the shock. As particles are advected away from the shock, they cool, primarily due to the emission of synchrotron and Compton radiation. Consequently, the highest energy particles, responsible for the emission near and beyond the peak of the synchrotron (and Compton) SED components, are expected to be concentrated in a small volume immediately downstream of the shock, where the shock-compressed magnetic field is expected to have a strong ordered (helical) component, in addition to shock-generated turbulent magnetic fields. Substantial degrees of polarization are thus expected near and beyond the peak of the synchrotron SED component. Due to progressive cooling of shock-accelerated electrons as they are advected downstream, the volume from which lower frequency synchrotron emission is received is expected to increase monotonically with decreasing frequency. One therefore expects a lower degree of polarization with decreasing frequency due to de-polarization from the superposition of radiation zones with different B-field orientations.

First of all, the general trend of a higher degree of polarization for GL compared to GQ AGNs may be explained as follows: GL AGNs (i.e. primarily blazars) are known to be highly variable, indicating a strong jet dominance throughout most of the SED due to a high degree of Doppler boosting (e.g. Savolainen et al. 2010; Lister et al. 2015) and the frequent occurrence of impulsive particle acceleration events, such as the shock-in-jet scenario described above. On the other hand, GQ AGNs appear to represent objects in which Doppler boosting is less extreme and/or impulsive particle acceleration episodes are less efficient, thus not accelerating particles to the energies required for gamma-ray production at measurable levels. Consequently, optical synchrotron emission is likely to be produced on larger volumes than in the more active GL objects, thus naturally explaining the lower degree of polarization.

This scenario also naturally explains the dependence of the degree of polarization on the synchrotron peak frequency. In LSP blazars, such as FSRQs and low-frequency peaked BL Lacs, the synchrotron peak frequency is typically located in the infrared. Thus, the optical regime represents the high-frequency portion of the synchrotron emission, for which – as elaborated above – one expects a high degree of polarization. In contrast, in HSP blazars, such as high-frequency peaked BL Lacs, the synchrotron peak tends to be located at UV or X-ray frequencies. Thus, here the optical regime represents the low-frequency part of the synchrotron SED, for which one expects a lower degree of polarization.

Finally, this scenario also explains the tendency of the optical EVPA rotation events to occur preferentially in LSP sources as we present elsewhere (Blinov et al., 2016b). In the case of LSP sources, the optical emission originates at the small volume in the immediately downstream environment of the shock, where the magnetic field has a strong helical component. In HSP sources on the other hand, the optical emission originates in a larger region farther downstream of the shock, where the electrons have already lost part of their energy and the turbulent B-field component becomes more significant. It has been shown by Blinov et al. (2015) and Kiehlmann et al. (2016) that two types of EVPA rotations may coexist in blazars. The smooth deterministic EVPA rotations may occur preferentially when plasmoids propagate through regions where the helical field component is dominant (e.g. Marscher et al. 2008, 2010; Zhang, Chen & Böttcher 2014; Zhang et al. 2015), whereas further downstream the EVPA variability is more likely to be driven by stochastic processes. Consequently, smooth rotations are more likely to occur in LSP than HSP sources. Indeed, all five rotations in fig. 8 of Blinov et al. (2015) associated with strong gamma-ray flares and short time lag from the flare, which are hence considered deterministic, have occurred in LSP sources. Moreover, the optical emission region in LSP sources is smaller than in HSP sources and thus expected to be more variable. In the context of stochastic variations, larger emitting region implies an increased number of cells, which decreases the variability (e.g. Kiehlmann et al. 2016). Also, the larger emission region in HSP sources increases the variability time-scale.

Assuming the superposition of a helical magnetic field component and a turbulent one, LSP and HSP sources may have an underlying, stable EVPA component due to the helical field component. In LSP sources, the stable component may not be clearly visible owing to stronger variability and shorter variability time-scales. In HSP sources, in which the variability amplitudes are lower and

variability time-scales are longer, the stable component may be more dominant. There, the combination of local turbulence that keeps the global magnetic field structure intact can explain a preferred, though slightly variable EVPA. Only long-term observations can confirm whether the EVPA has a truly preferred orientation on time-scales longer than the RoboPol observing periods.

If the difference between LSP and HSP sources in terms of polarization is indeed caused merely by the fact that observations in the optical band probe (a) regions of different size and (b) different parts of the particle distribution, then we would expect the same polarization variability in HSP sources at X-ray bands as in LSP sources in optical bands.

It is worth noting that in this scenario the rotations of the EVPA are expected to be happening downstream the shock in contrast to earlier suggestions (e.g. Marscher et al. 2010) that the region responsible for these events was just upstream of the shock.

ACKNOWLEDGEMENTS

The RoboPol project is a collaboration between Caltech in the USA, MPIfR in Germany, Toruń Centre for Astronomy in Poland, the University of Crete/FORTH in Greece, and IUCAA in India. The University of Crete group acknowledges support by the 'RoboPol' project, which is implemented under the 'Aristeia' action of the 'Operational Programme Education and Lifelong Learning' and is co-funded by the European Social Fund (ESF), Greek National Resources, the European Commission Seventh Framework Program (FP7) through grants PCIG10-GA-2011-304001 'JetPop' and PIRSES-GA-2012-31578 'EuroCal'. This research was also supported in part by NASA grant NNX11A043G and NSF grant AST-1109911, the Polish National Science Centre, grant number 2011/01/B/ST9/04618 and the COST Action MP1104 'Polarization as a tool to study the Solar System and beyond'. KT acknowledges support by the European Commission Seventh Framework Program (FP7) through the Marie Curie Career Integration Grant PCIG-GA-2011-293531 'SFOnset'. IM and SK were funded by the International Max Planck Research School (IMPRS) for Astronomy and Astrophysics at the Universities of Bonn and Cologne. MBa acknowledges support from the International Fulbright Science and Technology Award. TH was supported in part by the Academy of Finland project number 267324. We would also like to acknowledge partial support from the EU FP7 Grant PIRSES-GA-2012-316788. The work of MBo is supported by the South African Research Chair Initiative of the Department of Science and Technology and the National Research Foundation[3] of South Africa. This research has made use of the NASA/IPAC Extragalactic Database (NED) which is operated by the Jet Propulsion Laboratory, California Institute of Technology, under contract with the National Aeronautics and Space Administration. It also made use of ASTROPY, http://www.astropy.org, a community-developed core PYTHON package for Astronomy (Astropy Collaboration 2013). EA wishes to thank Dr R. Porcas and Dr F. Mantovani of the MPIfR for the fruitful discussions on the statistical behaviour of the polarization parameters, and the MPIfR internal referee Dr B. Boccardi for the constructive comments on the manuscript. Finally, EA wants to thank the anonymous referee for the careful reading and numerous insightful comments of the first manuscript.

[3] Any opinion, finding, and conclusion or recommendation expressed in this material is that of the authors, and the NRF does not accept any liability in this regard.

REFERENCES

Abdo A. A. et al., 2010, Nature, 463, 919
Acero F. et al., 2015, ApJS, 218, 23
Ackermann M. et al., 2015, ApJ, 810, 14
Ahn C. P. et al., 2012, ApJS, 203, 21
Aleksić J. et al., 2014, A&A, 567, A135
Andersson B.-G., Lazarian A., Vaillancourt J. E., 2015, ARA&A, 53, 501
Andruchow I., Cellone S. A., Romero G. E., 2008, MNRAS, 388, 1766
Astropy Collaboration, 2013, A&A, 558, A33
Blandford R. D., Königl A., 1979, ApJ, 232, 34
Blinov D. et al., 2015, MNRAS, 453, 1669
Blinov D. et al., 2016a, MNRAS, 457, 2252
Blinov D. et al., 2016b, MNRAS, 462, 1775
Burrows D. N. et al., 2005, Space Sci. Rev., 120, 165
Condon J. J., Cotton W. D., Greisen E. W., Yin Q. F., Perley R. A., Taylor G. B., Broderick J. J., 1998, AJ, 115, 1693
Dunlop J. S., McLure R. J., Kukula M. J., Baum S. A., O'Dea C. P., Hughes D. H., 2003, MNRAS, 340, 1095
Fiorucci M., Ciprini S., Tosti G., 2004, A&A, 419, 25
Fukugita M., Shimasaku K., Ichikawa T., 1995, PASP, 107, 945
Gregory P. C., Scott W. K., Douglas K., Condon J. J., 1996, ApJS, 103, 427
Hovatta T. et al., 2014, MNRAS, 439, 690
Kiehlmann S. et al., 2016, A&A, 590, A10
Kikuchi S., Mikami Y., Inoue M., Tabara H., Kato T., 1988, A&A, 190, L8
King O. G. et al., 2014, MNRAS, 442, 1706
Kirhakos S., Bahcall J. N., Schneider D. P., Kristian J., 1999, ApJ, 520, 67
Kotilainen J. K., Falomo R., Scarpa R., 1998, A&A, 332, 503
Kotilainen J. K., Hyvönen T., Falomo R., 2005, A&A, 440, 831
Lavalley M., Isobe T., Feigelson E., 1992, in Worrall D. M., Biemesderfer C., Barnes J., eds, ASP Conf. Ser. Vol. 25, Astronomical Data Analysis Software and Systems I. Astron. Soc. Pac., San Francisco, p. 245
Lister M. L. et al., 2011, ApJ, 742, 27
Lister M. L., Aller M. F., Aller H. D., Hovatta T., Max-Moerbeck W., Readhead A. C. S., Richards J. L., Ros E., 2015, ApJ, 810, L9
Mao P., Urry C. M., Massaro F., Paggi A., Cauteruccio J., Künzel S. R., 2016, ApJS, 224, 26
Marscher A. P. et al., 2008, Nature, 452, 966
Marscher A. P. et al., 2010, ApJ, 710, L126
Massaro E., Giommi P., Leto C., Marchegiani P., Maselli A., Perri M., Piranomonte S., Sclavi S., 2009, A&A, 495, 691
Massaro E., Maselli A., Leto C., Marchegiani P., Perri M., Giommi P., Piranomonte S., 2015, Ap&SS, 357, 75
Monet D. G. et al., 2003, AJ, 125, 984
Nilsson K., Pursimo T., Takalo L. O., Sillanpää A., Pietilä H., Heidt J., 1999, PASP, 111, 1223
Nilsson K., Pursimo T., Heidt J., Takalo L. O., Sillanpää A., Brinkmann W., 2003, A&A, 400, 95
Nilsson K., Pursimo T., Sillanpää A., Takalo L. O., Lindfors E., 2008, A&A, 487, L29
Nilsson K., Pursimo T., Villforth C., Lindfors E., Takalo L. O., 2009, A&A, 505, 601
Nolan P. L. et al., 2012, ApJS, 199, 31
Ofek E. O. et al., 2012, PASP, 124, 854
Pacholczyk A. G., 1970, Radio Astrophysics. Nonthermal Processes in Galactic and Extragalactic Sources, Freeman & Co., San Francisco
Panopoulou G. et al., 2015, MNRAS, 452, 715
Pavlidou V. et al., 2014, MNRAS, 442, 1693 (Survey Paper)
Richards J. L. et al., 2011, ApJS, 194, 29
Richards J. L., Hovatta T., Max-Moerbeck W., Pavlidou V., Pearson T. J., Readhead A. C. S., 2014, MNRAS, 438, 3058
Roy A. L., 1995, PASA, 12, 273
Saikia D. J., Salter C. J., 1988, ARA&A, 26, 93
Savolainen T., Homan D. C., Hovatta T., Kadler M., Kovalev Y. Y., Lister M. L., Ros E., Zensus J. A., 2010, A&A, 512, A24
Sazonov V. N., 1972, Ap&SS, 19, 25

Scarpa R., Urry C. M., Padovani P., Calzetti D., O'Dowd M., 2000, ApJ, 544, 258
Shaw M. S. et al., 2013, ApJ, 764, 135
Smith P. S., Allen R. G., Angel J. R. P., 1993, ApJ, 415, L83
Strittmatter P. A., Serkowski K., Carswell R., Stein W. A., Merrill K. M., Burbidge E. M., 1972, ApJ, 175, L7
Uemura M. et al., 2010, PASJ, 62, 69
Urry C. M., Scarpa R., O'Dowd M., Falomo R., Pesce J. E., Treves A., 2000, ApJ, 532, 816
van Dokkum P. G., Franx M., 1995, AJ, 110, 2027
Wardle J. F. C., Kronberg P. P., 1974, ApJ, 194, 249
White R. L., Becker R. H., Helfand D. J., Gregg M. D., 1997, ApJ, 475, 479
Wright A. E., Griffith M. R., Burke B. F., Ekers R. D., 1994, ApJS, 91, 111
Xiong D., Zhang X., Bai J., Zhang H., 2015, MNRAS, 450, 3568
Yuan J., Tran H. D., Wills B. J., Wills D., 1998, Am. Astron. Soc. Meeting Abstr. 30, 107.14
Zhang H., Chen X., Böttcher M., 2014, ApJ, 789, 66
Zhang H., Chen X., Böttcher M., Guo F., Li H., 2015, ApJ, 804, 58

APPENDIX A: CORRECTING FOR HOST GALAXY CONTRIBUTION

Host galaxy contribution magnitudes as well as limits have been sought in the literature for our all the sources in our sample. Most of the host galaxy magnitude estimates are obtained by modelling the core and galaxy emission using a de Vaucouleurs intensity profile integrated to infinity (e.g. Nilsson et al. 1999). Whenever the effective radius of the galaxy was available, we estimated the contribution of the host galaxy to our magnitude estimates by integrating up to 2.2 arcsec, the median aperture size in our observations using the equations described in Nilsson et al. (2009). Host galaxy magnitudes and limit measured in filters other than in the R band we converted between the magnitude systems by using average colour relations for elliptical galaxies from Kotilainen, Falomo & Scarpa (1998) and Fukugita, Shimasaku & Ichikawa (1995): $R - H = 2.5$, $H - K = 0.2$, and $R - I = 0.7$.

In Shaw et al. (2013), the absolute magnitude of the host galaxy is estimated from the spectra instead of fitting images. We convert their absolute magnitudes to apparent magnitudes using the cosmological parameters listed in their paper. The apparent R-band host galaxy magnitudes we use in our analysis are tabulated in Table A1. Altogether these were available for 38 objects in our sample, 33 of which are in the GL sample. The magnitude estimates include the correction for the finite aperture size and are not corrected for Galactic extinction.

For one of our sources, namely RBPLJ1203+6031, the host galaxy appears brighter than our mean observed magnitude. Its host estimate is taken from Shaw et al. (2013). It is then possible that the host galaxy estimates as computed from the spectra have larger systematic uncertainties than the estimates from direct imaging. We also do not account for the finite aperture size in our observations so that if the host is very extended, it may be that only a small portion falls within our aperture. The host estimate for RBPLJ1751+0939 is taken from Scarpa et al. (2000) where the imaging was done with an H-band filter. It is then possible that the typical elliptical galaxy colour we use to convert between the H- and R-band filters is not accurate for this source. For these sources, the host contribution correction is omitted.

The correction for the host galaxy contribution has been applied only to the luminosities. Formally, it should also be applied to the polarization fraction. However, the difference between the corrected and observed polarization fraction does not exceed the uncertainties in the polarization fraction. Therefore, we omit this correction.

Table A1. The host galaxy magnitudes for 33 GL sources. For one of these sources, the host magnitude estimate $m_{\rm host}$ is smaller than the mean magnitude of the target making the host contribution removal insensible.

ID (RBPL...)	$\langle R\rangle$ (mag)	$R_{\rm host}$ (mag)	Reference	ID (RBPL...)	$\langle R\rangle$ (mag)	$R_{\rm host}$ (mag)	Reference	ID (RBPL...)	$\langle R\rangle$ (mag)	$R_{\rm host}$ (mag)	Reference
J0217+0837	15.75	16.46	1	J1217+3007	14.16	17.49	5	J1751+0939	15.90	16.32	9
J0339−0146	16.67	19.10	2	J1229+0203	12.28	17.25	2	J1800+7828	15.46	17.12	8
J0423−0120	17.77	20.32	2	J1248+5820	15.11	21.20	4	J1806+6949	14.43	16.05	5
J0721+7120	14.31	18.20	3	J1256−0547	14.87	20.00	6	J1813+3144	16.38	18.85	5
J0738+1742	15.15	20.44	4	J1427+2348	13.87	21.00	4	J1824+5651	16.19	20.85	5
J0818+4222	17.85	21.47	4	J1512−0905	15.50	18.70	2	J1838+4802	15.56	19.48	5
J0854+2006	14.88	18.10	5	J1555+1111	13.97	21.60	4	J1959+6508	14.03	16.28	4
J0958+6533	16.30	19.60	5	J1642+3948	17.30	20.22	7	J2005+7752	15.95	20.47	4
J1058+5628	15.51	16.86	1	J1653+3945	13.73	14.85	5	J2143+1743	15.65	18.53	10
J1132+0034	17.02	20.45	1	J1725+1152	14.45	21.40	4	J2202+4216	13.05	16.82	5
J1203+6031	15.73	15.34[a]	1	J1748+70 05	14.90	18.24	8	J2251+4030	16.50	17.99	1

[a] $R_{\rm host} < \langle R\rangle$.

References – 1: Shaw et al. (2013), 2: Kotilainen et al. (1998), 3: Nilsson et al. (2008), 4: Urry et al. (2000), 5: Nilsson et al. (2003), 6: Nilsson et al. (2009), 7: Kirhakos et al. (1999), 8: Kotilainen, Hyvönen & Falomo (2005), 9: Scarpa et al. (2000), 10: Dunlop et al. (2003).

This paper has been typeset from a TEX/LATEX file prepared by the author.